ČESKÉ VYSOKÉ UČENÍ TECHNICKÉ

FAKULTA JADERNÁ
A FYZIKÁLNĚ INŽENÝRSKÁ

Post komprese energetických laserových impulsů pro generaci vysokých harmonických

Diplomová práce

Autor: **Bc. Ondřej Sedláček**
Vedoucí: **Ondřej Hort, Ph.D.**
Konzultant: **Ing. Michal Jelínek, Ph.D.**

2022/2023

Abstract

Post komprese energetických laserových impulsů pro generaci vysokých harmonických

Ultra krátké pulzy, obvykle trvající desítky nebo stovky femtosekund jsou klíčovým nástrojem pro výzkum elektronové dynamiky. Nicméně některé pokročilé aplikace vyžadují ještě kratší pulzy. Few-cycle pulzy, sestávající se pouze z 2-3 period tomuto vyhovují, avšak mají i další výhody. Jejich hlavní výhoda spočívá v tom, že špičková intenzita je dosažena téměř okamžitě, v průběhu jednoho optického cyklu. Tím umožňují například efektivnější generaci vysokých harmonických, nebo využít takzvaný carrier-envelope offset, čímž je zvýšena míra kontroly na pulzem.

Fundamentální překážka nám však brání v generování few-cycle pulzů přímo laserem. Nejkratší možná délka pulzu je dána jeho spektrální šířkou, která je zase převážně určena aktivním médiem laseru. Aby bylo možné toto omezení překonat, je nutné nejdřív rozšířit spektrum. Toho lze dosáhnout zpětně, poté co pulz opustí laser, a to pomocí nelineární interakce s médiem. To je základní idea, na které stojí technika post komprese.

V této práci připravujeme experimentální sestavu pro post kompresi s cílem generovat few-cycle pulzy. Návrh experimentu počítá s využitím dvou různých nelineárních jevů pro rozšíření spektra, a sice ionizaci optickým polem a Kerrovým jevem indukovanou automodulaci. Cílem je sestavit zařízení, které bude schopné se vypořádat s extrémně vysokým špičkovým výkonem v řádu terawattů.

Klíčová slova

post komprese, few-cycle pulz, ionizací indukované rozšíření spektra

Abstract

Post-compression of high-energy femtosecond laser pulses for high-order harmonic generation

Ultra-short pulses, typically with duration in tens or hundreds of femtoseconds, are the key tool for the research of electron dynamics. However, in some cases, even shorter pulses are required. Few-cycle pulses, consisting of only 2-3 periods, satisfy this requirement, however, they have more to offer apart from being extremely short. The main advantage is linked to the fact that the peak intensity is reached almost immediately, over the course of a fraction of an optical cycle. This allows for example to generate HHG more efficiently, or exploit carrier-envelope offset, exerting additional control over the pulse properties.

However, a fundamental obstacle prevents us from generating few-cycle pulses from the laser directly. The shortest possible duration of a pulse is given by its bandwidth, which in turn is given mostly by the active medium of the laser. One would first need to broaden the pulse spectrum to overcome this limitation. That can be achieved ex post, after the pulse leaves the laser, via non-linear interaction with a medium. This is the fundamental idea behind the post-compression technique.

In this work, we prepare a setup for a post-compression experiment, with the aim to generate few-cycle pulses. The experiment is designed to exploit two different non-linear phenomena for spectral broadening purposes, optical field ionization, and Kerr effect-induced self-phase modulation. The goal is to build a device able to deal with extremely high peak power in the terawatt region.

Key words

post-compression, few-cycle pulse, ionization-induced spectral broadening

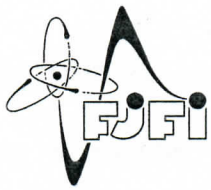

ČESKÉ VYSOKÉ UČENÍ TECHNICKÉ V PRAZE

FAKULTA JADERNÁ A FYZIKÁLNĚ INŽENÝRSKÁ

Katedra fyzikální elektroniky

ZADÁNÍ DIPLOMOVÉ PRÁCE

Student:	**Bc. Ondřej S e d l á č e k**
Studijní program:	**Fyzikální elektronika**
Specializace:	**Laserová fyzika a technika**
Akademický rok:	**2022/2023**
Název práce: (česky)	**Post komprese energetických laserových impulsů pro generaci vysokých harmonických**
Název práce: (anglicky)	**Post-compression of high energy femtosecond laser pulses for high-order harmonic generation**
Jazyk práce:	**Angličtina**

Cíl práce:

Připravte implementaci experimentu post komprese pro lasery v hale E1 na ELI Beamlines. Ověřte, že pomocí této techniky lze zkrátit délku impulsu ze 40 fs na dva optické cykly a z 15 fs na jeden cyklus a tím zvýšit špičkový výkon.

Pokyny pro vypracování:

1. Proveďte výpočet výsledných parametrů post-komprimovaných impulzů.
2. Sestavte a nainstalujte experimentální sestavu vedení laserového svazku v hale E1.
3. Navrhněte nezbytnou laserovou diagnostiku, nainstalujte a otestujte ji.

Doporučená literatura:

1. Hort O., High harmonic generation with high energy femtosecond pulses, disertační práce, Université de Bordeaux, 2014.
2. Farace B., Post-compression of high energy femtosecond pulses, diplomová práce, Politecnico di Milano, 2020.
3. Boyd R., Nonlinear Optics, 3rd Edition. Academic Press, 2008.
4. Auguste T. et al., High-energy femtosecond laser pulse compression in single- and multiionization regime of rare gases: experiment versus theory, Applied Physics B 111:75-87,
5. 2013.
6. Tong X. M. and Lin C. D., Empirical formula for static field ionization rates of atoms and molecules by lasers in the barrier-suppression regime, Journal of Physics B: Atomic, Molecular and Optical Physics 38:2593-2600, 2005.

Jméno a pracoviště vedoucího práce:

Ondřej Hort, Ph.D.
FzÚ AV ČR, v.v.i., ELI Beamlines

Jméno a pracoviště konzultanta:

Ing. Michal Jelínek, Ph.D.
Katedra fyzikální elektroniky, Fakulta jaderná a fyzikálně inženýrská ČVUT v Praze

Datum zadání: 12. říjen 2022

Datum odevzdání: 3. květen 2023

Doba platnosti zadání je dva roky od data zadání.

.....

Garant programu

....

Vedoucí katedry *Děkan*

ČESKÉ VYSOKÉ UČENÍ TECHNICKÉ V PRAZE Fakulta jaderná a fyzikálně inženýrská -3-

V Praze dne 12.10.2022

Prohlášení

Prohlašuji, že jsem předloženou práci vypracoval samostatně a že jsem uvedl veškerou použitou literaturu.

V Praze dne 2.5.2022 Ondřej Sedláček

Poděkování

Rád bych poděkoval vedoucímu této práce Ondřeji Hortovi, Ph.D. za trpělivost, ochotu a cenné rady, které mi při vypracování diplomové práce poskytl.

Contents

Chapter 1

Introduction

High-order harmonic generation (HHG) is a fascinating phenomenon in the field of ultrafast laser physics, which has gained significant attention over the last few decades. This process involves the generation of coherent extreme ultraviolet (XUV) and soft X-ray radiation from the interaction of a high-power femtosecond laser pulse with a gas target. HHG has numerous applications in areas such as spectroscopy, material science, and imaging.

However, one of the major challenges in HHG is the production of high-energy XUV pulses with a sufficient peak power to enable advanced applications. Post-compression of high-power femtosecond laser pulses is a widely used technique to achieve this goal. This technique enables us to modify laser pulses that are already Fourier-limited and make them even shorter by manipulating their spectral phase. By doing so, we can generate few-cycle pulses with high peak power, which are essential for efficient HHG.

The primary objective of this Master's thesis is to investigate the post-compression of high-power femtosecond laser pulses for high-order harmonic generation. This thesis will involve the calculation of the necessary parameters for the output pulses, including the pulse duration, energy, and peak power. Additionally, the thesis aims to design and build an experimental setup in the E1 hall and install the necessary diagnostic tools to test the output pulses.

The experimental setup will involve the use of a chirped pulse amplification system to generate high-power femtosecond laser pulses, which will be compressed using a post-compression stage. The device, once completed, will be used to generate high-order harmonics through the interaction with a gas target.

Overall, this Master's thesis aims to contribute to the advancement of high-order harmonic generation by investigating the post-compression of high-power femtosecond laser pulses. The thesis will provide valuable insights into the generation of high-energy XUV pulses, which will have significant implications for applications in spectroscopy, material science, and imaging.

Chapter 2

Fundamental principles

2.1 Non-linear optics

A classical description of the interaction between a medium and an electromagnetic wave is modeled via an atom (or more precisely, a center of charge) oscillating in the wake of the alternating electric field, subsequently generating another electromagnetic wave. In most cases, the restoring force acting on the electron is proportional to the first power of displacement and the response is linear, therefore the electron can be described as a driven harmonic oscillator. According to the equations of motion, the displacement is linearly proportional to the driving field amplitude. This is an important observation, as the displacement of an electric charge is simply polarization, so the wave equation describing the interaction is as follows:

$$\nabla^2 E - \frac{1}{c^2}\frac{\partial^2 E}{\partial t^2} = \mu_0 \frac{\partial^2 P}{\partial t^2} \tag{2.1}$$

Here E denotes the electric field amplitude, c denotes the speed of an electromagnetic wave in vacuum, μ_0 denotes vacuum permeability and P denotes polarization. The left-hand side describes the propagation of the EM wave, while the right-hand side represents the response of the medium. As it was implied, the relationship between P and E is linear and it is usually described as follows:

$$P = \epsilon_0 \chi^{(1)} E \tag{2.2}$$

Here ϵ_0 is vacuum permitivity and $\chi^{(1)}$ is a quantity called linear susceptibility.

In this simplified explanation, we have assumed that $E(t)$ and $P(t)$ are scalar, while in reality, they are vector quantities. We also assume that $\chi^{(1)}$ is a proportionality constant, while in reality, it is a frequency-dependent, complex function. The simplified theory is presented here to give insight into the source of the processes we will be dealing with, and for these purposes it is sufficient. For better insight with a rigorous explanation of the vector

nature of the fields and the dispersive nature of the susceptibility with regard to nonlinear optics, we refer the reader to a more dense literature [1].

Once the driving force becomes sufficiently high, the displacement ceases to be linearly proportional to it. The polarization becomes a complicated function, however, we can write it as a Taylor expansion:

$$P(t) = \epsilon_0 \chi^{(1)} E(t) + \epsilon_0 \chi^{(2)} E^2(t) + \epsilon_0 \chi^{(3)} E^3(t) + ... \tag{2.3}$$

Where $\chi^{(2)}$ is second order susceptibility, $\chi^{(3)}$ third order and so on. To simplify notation, higher-order polarization is often defined, so that

$$\epsilon_0 \chi^{(i)} E^i(t) = P^{(i)} \tag{2.4}$$

denotes polarization of *i-th* order, hence

$$P(t) = P^{(1)} + P^{(2)} + P^{(3)} + ... \tag{2.5}$$

It is the higher-order polarization terms, that are responsible for the generation of new frequencies. The simplest example on which we can demonstrate this is an effect called second harmonic generation. Let us have an electromagnetic wave with an amplitude

$$E(t) = E_0 e^{-i\omega t} + E_0^* e^{i\omega t} \tag{2.6}$$

Substituting into equation 2.4 for the case of second-order polarization, we get

$$P^{(2)} = \epsilon_0 \chi^{(2)} (2E_0 E_0^* + E_0^2 e^{-i2\omega t} + E_0^{*2} e^{i2\omega t}) \tag{2.7}$$

Here it can be seen clearly that the second-order polarization is oscillating with double the frequency of the driving field, therefore it can be a source of electromagnetic radiation at such frequency.

In the example above, we have considered only second-order polarization, which is directly linked with second-order susceptibility. However, exactly the same reasoning is true for higher-order susceptibilities as well. For example, it can be shown that the third-order susceptibility is responsible for the generation of triple the frequency and so on.

However, there is an important distinction to be made. While it is true that for high intensities of the driving force (i.e. electric field,) the polarization is not linearly proportional to the field intensity, there is a fundamental difference between odd and even orders. For even orders, the restoring force acting on the electron is proportional to the even order polynomial (as a function of displacement). Consequently, the potential in which the particle is located must be a polynomial of odd order, therefore it is an asymmetrical function. This means that even order susceptibilities can only be present in media that lack central symmetry. On the other hand, exactly the opposite is true for odd-order susceptibilities. Therefore it is convenient to separate all processes and media linked with even orders from odd orders. It is customary to call all even order processes χ^2 and all odd order process χ^3.

It should be noted that for simplification, we have only discussed the degenerate case. In the example above, the two waves of the same frequency are coupled, generating another wave of double the frequency. However, in the general case, this process can occur between two waves of different frequencies that add up together. Such a process is called sum frequency generation. In reality, the limiting factor is the law of conservation of energy. Analyzing the conditions under which it is fulfilled, we conclude that another solution is the case when the frequency of one wave is subtracted from the frequency of another wave, resulting in a process called difference frequency generation. This is true even in the degenerate case, where a quasi-DC polarization is generated in a process called optical rectification. By applying the same reasoning to higher-order susceptibilities, we obtain numerous other processes. In the next part, we shall describe those relevant to the technique of post-compression.

2.2 Kerr effect

Kerr effect is a special degenerate case of a χ^3 process. In this case, energy conservation is fulfilled as follows:

$$\hbar\omega_1 = \hbar\omega_1 + \hbar\omega_2 - \hbar\omega_2 \tag{2.8}$$

This 4-wave interaction produces a wave at the output, that has the same frequency as the wave on the input. While no new frequencies are generated directly, they are generated through a process called self-phase modulation (SPM).

2.2.1 Self-phase modulation

Applying an electric field to medium results in a change in the refractive index, with the change being proportional to the intensity of the field. This process was discovered by Scottish physicist John Kerr in the nineteenth century and it is indeed the same process as the one described above. For the effect to be noticeable, the intensity of the electric field must be sufficiently high, as the change in refractive index is described as

$$n = n_0 + I \cdot n_2 \tag{2.9}$$

where n_0 is the standard refractive index, I is electric field intensity and n_2 is a medium dependent constant, which is usually a very small number.

The intensity of a laser pulse is not constant over the duration of the pulse, therefore the refractive index also varies over time. The temporal variation of the refractive index is the source of new frequencies. This process is called self-phase modulation (SPM).

Let us consider a simple 1D case. The phase of the laser pulse is described as

$$\varphi(z,t) = \omega_0 t - kz \tag{2.10}$$

where ω_0 is the frequency of the pulse, would it propagate through a vacuum, and k is the wavenumber, which can be rewritten as

$$k = \frac{\omega_0 \cdot n}{c} \tag{2.11}$$

After substituting to 2.10, we get

$$\varphi(z,t) = \omega_0 \left(t - z\frac{n(z,t)}{c} \right) \tag{2.12}$$

The frequency is defined as a temporal change of the phase, which gives us

$$\omega(z,t) = \omega_0 - \frac{\omega_0 z}{c}\frac{\partial n(z,t)}{\partial t} \tag{2.13}$$

We can see that the frequencies generated are proportional to the temporal change of the refractive index. Finally, substituting for refractive index from equation 2.9, we obtain:

$$\omega(z,t) = \omega_0 \left(1 - \frac{z n_2}{c} \frac{\partial I(z,t)}{\partial t}\right) \tag{2.14}$$

Therefore the generated frequencies are proportional to the negative rate of change of the intensity, as illustrated in 2.1.

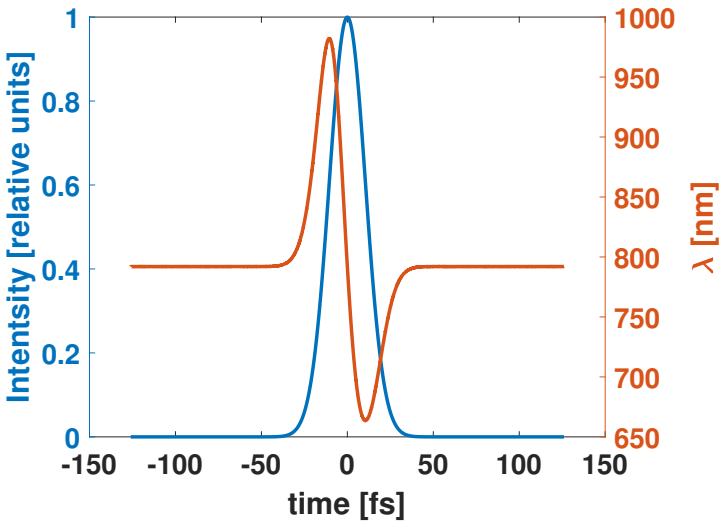

Figure 2.1: New wavelengths generated due to Kerr effect

Here we are assuming a pulse with intensity $I = 2.8 \cdot 10^{14} W/cm^2$, propagating in 0.7 bar of helium. The parameters have been chosen somewhat arbitrarily since the graph is meant solely for illustrative purposes.

A useful quantity is the so-called B-integral. It indicates the amount of phase shift acquired due to the Kerr effect. It is given as:

$$B = \frac{2\pi}{\lambda} \int_0^L n_2 I(z) dz \tag{2.15}$$

Here λ is the laser wavelength, n_2 is the non-linear refractive index, I is the laser intensity, and L is the length of the non-linear medium. It is useful not only to quantify the amount of spectral broadening but also relates to the phenomenon of self-focusing, which shall be introduced next.

2.2.2 Kerr lensing

Kerr lensing is another phenomenon which occurs as a result of the Kerr effect. Here the key element is the transverse profile of power in the laser beam.

For simplicity, let us suppose the beam is Gaussian. For high enough intensity, the non-linear refractive index comes into play. Recalling equation

2.9, we can see that higher intensity results in a higher refractive index. Therefore the refractive index is higher at the centre of the beam. This is also the case for a standard converging lens, where the glass is thicker in the centre. Indeed, in both cases, the consequence is the convergence of the beam. The effect is illustrated in image 2.2. Therefore we conclude that a medium with a sufficiently high non-linear refractive index (or for intense enough beam) acts as a converging lens.

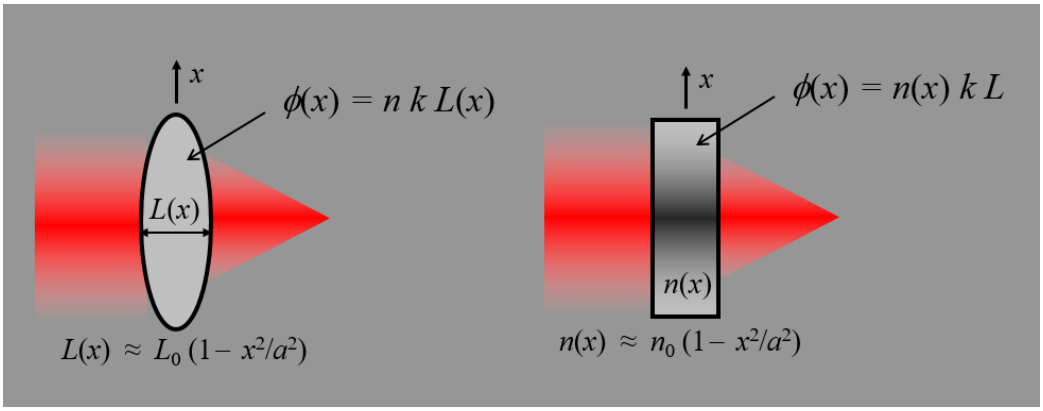

Figure 2.2: A standard lens and a Kerr lens [10]

This can sometimes be useful, for example in resonators of Ti:sapphire lasers, but in our case, it will prove to be a limiting factor. First, let us consider a low-power laser beam propagating through a medium. The diffraction causes the beam to diverge slightly. If we increased the power of the laser, eventually the Kerr effect would become apparent and the beam would diverge ever so slightly less, as the Kerr lensing would partly compensate for the diffraction-induced divergence. Should we increase the power even more, we would come to a point where the Kerr lensing perfectly compensates for the diffraction. This threshold is called the critical power P_c, and it is important because it separates two regimes [11].

Should we increase the power further yet, the beam becomes convergent, providing positive feedback for the Kerr effect. As the beam converges, the intensity at the centre becomes higher, further increasing the influence of the non-linear refractive index, resulting in higher convergence. As we are already dealing with high intensities, at some point the ionization threshold is inevitably crossed.

When ionization occurs the refractive index will decrease. The index will change according to the following equation:

$$n(z,t) = \sqrt{1 - \frac{n_e(z,t)}{n_c}} \tag{2.16}$$

where n_e is free electron density and n_c is critical electron density given as $n_c = \frac{m_e \epsilon_0 \omega^2}{e^2}$, where m_e is electron mass, ϵ_0 is vacuum permitivity, ω is the laser frequency and e is elementary charge.

The highest intensity near the centre of the beam will result in a higher density of free electrons, which in turn will produce a lower refractive index. This process is therefore opposite to Kerr lensing in the sense that it creates a diverging lens. This will then cause the beam to expand and intensity gets lower once again. Eventually, the medium ceases to be ionized and the process may repeat. This process is called filamentation and it is linked with energy loss and beam deterioration. Hence in our application, we will try not to cross the critical power.

2.3 Optical field ionization

As it was mentioned in the previous part, when power gets high enough, ionization occurs. The electron can become free thanks to the change of the shape of the potential well due to the laser electric field, therefore it is called optical field ionization (OFI). Several different regimes are recognized. We shall introduce those linked with strong fields, where the electric field becomes comparable with the potential binding the electron to its parent ion.

The main factors determining the nature of the process are the ionization potential and ponderomotive energy. Ionization potential I_p is the energy required to split off the electron. Ponderomotive energy U_p is the average kinetic energy of the oscillations of a free electron in a laser field [12]. These quantities are linked through a dimensionless Keldysh parameter:

$$\gamma = \sqrt{\frac{I_p}{2U_p}} \tag{2.17}$$

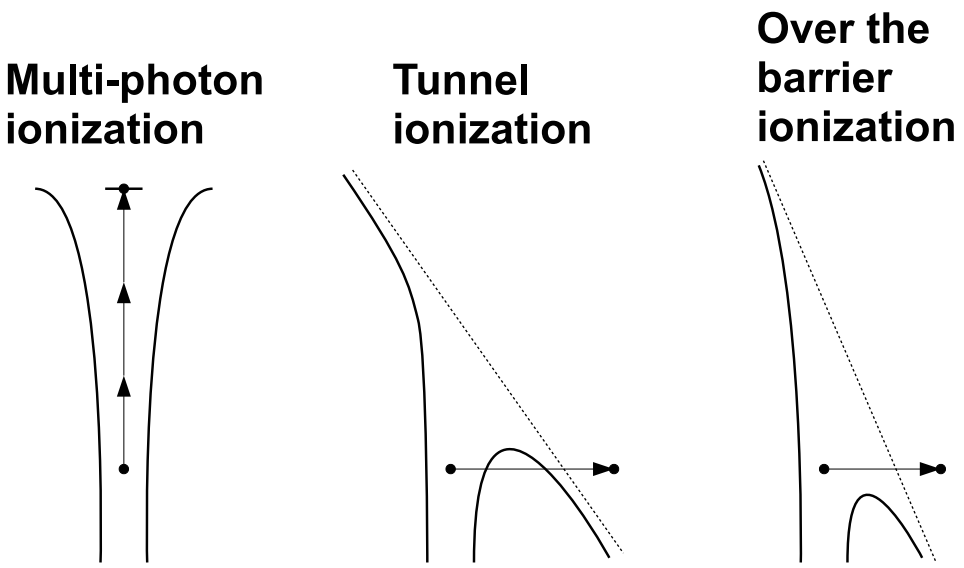

Figure 2.3: Illustrative depiction of different regimes of optical field ionization

While ionization energy is a constant determined by the atom (different elements have different ionization energies), the ponderomotive energy is given by the laser field amplitude and frequency:

$$U_p = \frac{e^2 E^2}{4 m_e \omega^2} \tag{2.18}$$

where e is elementary charge, E is electric field amplitude, m_e is electron mass and ω is the laser frequency.

Depending on the medium and laser parameters, we recognize multi-photon ionization (MPI), tunnel ionization (TI), and over-the-barrier ionization (OTBI).

Multi-photon ionization is described as a process in which the electron absorbs multiple photons at once, eventually reaching a continuum. Compared to the other regimes mentioned, it is characterized by relatively lower laser intensities or higher frequencies. In terms of the Keldysh parameter, the process is usually considered to be a multi-photon ionization for $\gamma > 1$.

Single-photon is a special case of multi-photon ionization, in which a single photon carries enough energy to excite the electron and reach the continuum.

Tunnel ionization on the other hand is described via the deformation of the potential well. This creates a barrier through which the electron has a finite chance to tunnel. The stronger the field the thinner the barrier, and the higher the chance. This process contrary to the two previous examples is characterized by a stronger field and lower laser frequency. The process is considered to be a tunnel ionization for $\gamma < 1$.

Over-the-barrier ionization is similar to tunnel ionization, however, the field here is strong enough that the barrier diminishes completely. This effectively cancels the potential well, freeing the electron. It is linked with $\gamma << 1$.

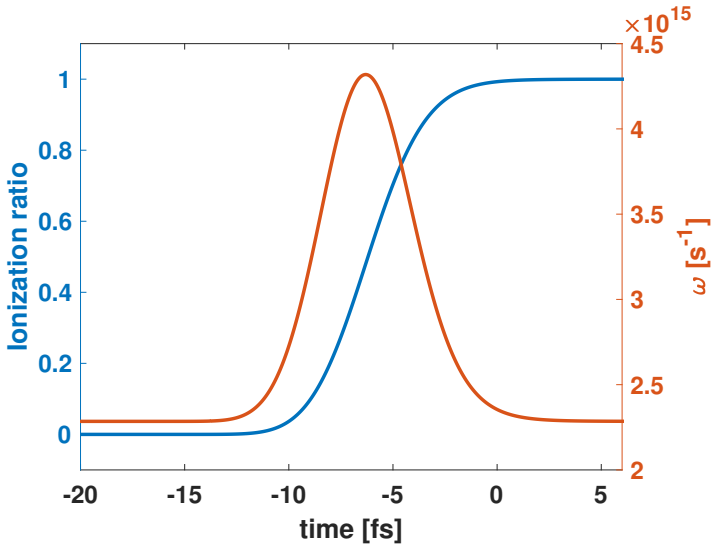

Figure 2.4: Frequencies generated in gaseous medium due to rapid OFI

2.3.1 Ionization induced SPM

As it was mentioned in the previous chapter, ionization is always linked with the change in the refractive index. The change is given by equation 2.16. Let us suppose the ionization is a rapid process, comparable to the duration of the

pulse. As was shown in the previous section, the ensuing temporal variation of the refractive index results in self-phase modulation. With temporally variable free electron density, after substituting equation 2.16 into equation for phase 2.10 we get:

$$\varphi(z,t) = \omega_0 t - \frac{\omega_0 z}{c}\sqrt{1 - \frac{n_e(z,t)}{n_c}} \tag{2.19}$$

As in the previous case, the frequency is just a temporal change of the phase, so it is given as

$$\omega(z,t) = \omega_0 \left(1 + \frac{z}{c\sqrt{1 - \frac{n_e(z,t)}{n_c}}}\frac{\partial n_e(z,t)}{\partial t}\right) \tag{2.20}$$

The image 2.4 shows how new frequencies are generated based on the change of the free electron density in time. Here we assume a pulse with intensity $I = 5 \cdot 10^{15} W/cm^2$ propagating in 8 mbar of helium. However the parameters have been chosen somewhat arbitrarily since the graph is meant solely for illustrative purposes.

2.4 Dispersion

Dispersion is an ever-present effect, linked with the frequency dependence of the wavevector k on frequency ω. It is relevant for post-compression because spectral broadening introduces dispersion that needs to be compensated. During the non-linear propagation, a so-called chirp is introduced to the pulse. This term is linked with the spectral phase, and it also directly relates to dispersion.

Dispersion describes the dependence of the wavevector k on frequency ω. We take the Taylor polynomial of this function:

$$k(\omega) = k_0 + \frac{\partial k}{\partial \omega}(\omega - \omega_0) + \frac{1}{2}\frac{\partial^2 k}{\partial \omega^2}(\omega - \omega_0)^2 + ... \tag{2.21}$$

The term $\frac{\partial k}{\partial \omega}$ corresponds to the inverse of group velocity, and it determines the velocity at which the pulse envelope will propagate. The term $\frac{\partial^2 k}{\partial \omega^2}$ is called group velocity dispersion (GVD), and it describes how the group velocity depends on frequency. When it is non-zero, each spectral component propagates with a different velocity, altering the shape of the envelope.

The basic unit of GVD in SI is s^2/m, but for practical reasons a different unit is typically used. The quantity describes the delay introduced by the medium between two spectral components per unit length. If we multiply it by the medium length L, we obtain a new quantity called group delay dispersion (GDD):

$$GDD = GVD \cdot L \tag{2.22}$$

The basic unit of GDD is then s^2, although s/Hz may appear more intuitive, as it highlights the role of the bandwidth. In the ultrafast industry, however, it is customary to use fs^2.

2.4.1 Chirp

A pulse can be described either in the temporal or spectral domain. These two representations are connected through the Fourier transform. In the temporal domain, the electric field $E(t)$ is given as

$$E(t) = \mathrm{Re}\{\sqrt{I(t)}\exp\left[-i\left(\omega_0 t - \phi(t)\right)\right]\} \tag{2.23}$$

Here the intensity $I(t)$ is responsible for the shape of the envelope, while the phase $\phi(t)$ determines the carrier frequency. In the reciprocal space, the field $E(\omega)$ is given as

$$E(\omega) = \sqrt{S(\omega)}\exp\left[i\varphi(\omega)\right] \tag{2.24}$$

where $S(\omega)$ is spectrum and the spectral phase $\varphi(\omega)$ determines the relative shift of the spectral components.

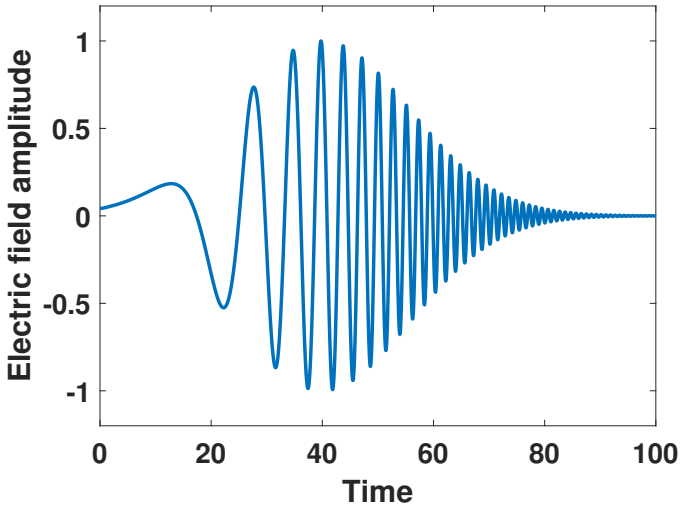

Figure 2.5: A chirped pulse. Units are arbitrary.

Flat (constant) spectral phase results in constructive interference in one spot and destructive interference everywhere else, yielding the shortest possible pulse. The linear spectral phase will manifest in the temporal domain as a simple shift of the pulse in time. However quadratic spectral phase will cause desynchronization of the spectral components, as seen in image 2.5. This will alter the shape of the envelope, making the pulse longer. The quadratic spectral phase can be identified with the GDD from the previous section, as it holds:

$$GDD = \frac{\partial^2 \varphi(\omega)}{\partial \omega^2} \tag{2.25}$$

Since the instantaneous frequency changes in time, the effect is called chirp, with an analogy to bird chirping. We distinguish between up-chirp, in which case the frequency increases, and down-chirp, where the frequency decreases. Oftentimes, the pulse can experience a combination of multiple up-chirps and down-chirps. This can be nicely seen in the example of the two processes used for spectral broadening in our experiment.

In the case of ionization, the frequencies generated are proportional to the rate of change of the ionization ratio, which is a monotonous function. Therefore the broadening occurs towards higher frequencies and the spectrum is blue-shifted. The front of the pulse experiences an up-chirp, as the frequency is increasing, with the opposite being true for the trailing edge.

In the case of Kerr effect-induced SPM, the situation is even more complicated. At the leading edge, the intensity is rising fast, therefore the spectrum is red-shifted and the pulse is down-chirped. Then the rate of change of intensity decreases, at the peak of the pulse the rate of change is zero. This means that the frequency is increasing, therefore we get up-chirp. As we get to the trailing edge, the intensity plummets and the spectrum becomes blue-shifted,

resulting in more up-chirp. Finally, at the bottom half of the trailing edge, the rate of change is decreasing. As the instantaneous frequency returns to its central value, the pulse is down-chirped once more.

2.5 Dispersion compensation

With the exception of anomalous dispersion, all materials produce positive GDD. Hence dispersion compensation is mostly linked with introducing a negative GDD. That is not as simple as it may seem at first glance. Negative GDD is always produced by anomalous dispersion, which only occurs at the resonant frequency, leading to high absorbive losses. It is impossible to find a material that would introduce negative GDD for dispersion compensation and wouldn't be lossy at the same time. A different approach is required. Three techniques have been developed and are in use today to get negative GDD.

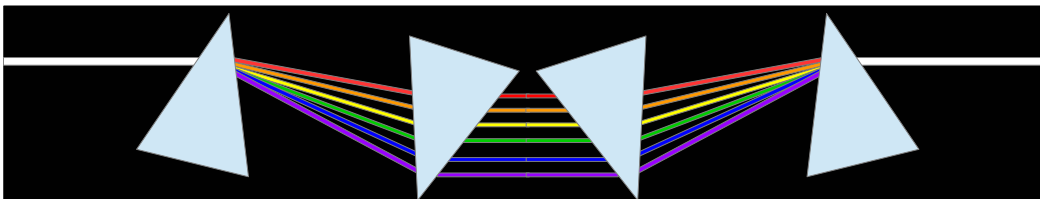

Figure 2.6: Prism compressor

2.5.1 Prism compressor

As it turns out, the problem can be translated into the spatial domain. A light passing through a glass prism will cause spatial dispersion, splitting the pulse to its spectral components. By arranging multiple prisms in a specific way, we can introduce different path lengths to each component. After passing through the last prism, the components are joined back together, but they are delayed from each other. The principle is illustrated in image 2.6. Alternatively, the device works with only two prisms, with the second half of the compressor being replaced by a flat mirror.

The advantage of this compressor (in either arrangement) is relatively simple tunability. That is achieved by simply pushing one of the prisms further into the beam, changing the amount of dispersion and therefore the path length between the components. The main disadvantage is its inability to deal with higher-order dispersion, which means the bandwidth over which the prisms work efficiently is limited. Moreover, unwanted non-linearities will occur if a high peak-power pulse should propagate through it. These two facts make this device unsuitable for our purposes.

2.5.2 Grating compressor

The grating compressor utilizes the same principle as the prism compressor, but with gratings being responsible for splitting the spectral components. It

suffers from the same issue of not being able to deal with higher-order dispersion, therefore the bandwidth is limited. Another issue is its low throughput, which is usually $< 75\%$ [2].Most importantly, it introduces a very high amount of negative GDD. This would cause overcompensation. To introduce less GDD, the gratings would have to be close to each other, so much so that the beam would not fit between them. These facts make this method unsuitable for our purposes.

2.5.3 Chirped mirrors

Chirped mirrors work on the principle of Bragg reflector, where periodically alternating layers create wavelength-specific mirrors. The reflected wavelength λ_{ref} is

$$\lambda_{ref} = 2n_{eff}d \tag{2.26}$$

where n_{eff} is the effective refractive index of the alternating layers, and d is their thickness. By varying the thickness of the layers, we can finely tune the depth to which each wavelength penetrates.

Two problems need to be addressed. Firstly, there is a strong Fresnel reflection at the air-mirror interface. This creates additional dispersion, which is undesirable. Second, there is an issue with impedance mismatch due to a jump at the interface in the value of coupling between the two counter-propagating waves. Both of these issues create oscillation in GDD. The solution is to use the chirped mirror pairs with complementary coatings. However, this approach is prone to manufacturing errors. Improved design uses pairs where the mirrors have the same coating, but the angle of incidence is slightly different. This not only removes the GDD oscillations but also allows tuning of the sum GDD curve [3]. Innovative layer designs based on numerical simulations are used to further mitigate any remaining oscillations, as well as additional anti-reflective coatings.

2.5.4 Pulse recompression

As it was shown, broadening the pulse spectrum introduces chirp, which means the pulse itself gets longer. To actually achieve compression, one must compensate for the dispersion by introducing a specific amount of GDD. Of course, the fact that each part of the pulse experiences a different chirp complicates the matter. It is not possible to selectively apply different corrections to different parts of the pulse.

In reality, usually, only negative GDD is applied [4]. This means that the recompression is not perfect, but it has been shown that significant pulse compression is achievable nonetheless. This is an issue mostly for the case of ionization broadening only. While in the case of SPM the pulse experiences up-chirp as well as down-chirp, most of the energy is present in the part that experiences up-chirp (as seen in image 2.1).

Chapter 3

Post-compression state of the art

This chapter is devoted to an overview of the current experiments involving high-energy post-compression. There are numerous methods used to broaden the spectrum. They always involve one of the phenomena mentioned in the previous chapter. Most methods are based on some sort of waveguide.

One of the possibilities is to use solid-state fibers. These can be based either on total internal reflection, or they can be photonic crystals. In either case, the fiber is usually made to support a single mode, minimizing the losses. This allows for great fiber lengths, increasing the B-integral. The obvious limitation is the low damage threshold of the medium, making it useful only for the lowest of energies.

Another option is to use hollow core fiber. It is a thin silica capillary, usually a few tens of centimeters long. The main advantage of this method is its ability to deal with high energies. On the other hand, we must remember that the propagation fundamentally differs from the previous case. Here it is realized by reflections under grazing angles. The propagation is also inherently multimode, as manufacturing a capillary with an inner diameter able to support single-mode propagation is currently beyond technical possibilities. Both of these facts make high demands on the capillary straightness, as the slightest bend will lead to losses linked with the propagation of more lossy modes.

Another method relies on propagation through a multi-pass cell. Here the beam passes multiple times through a medium, which can be either bulk or gas. While good results were achieved with this method [5], scaling to high-energy pulses is yet to be demonstrated.

Hollow core fiber seems to be the optimal solution, begin able to deal with high intensities. Indeed, it has been the workhorse of post-compression for a couple of the past years. There are still multiple possibilities for how to employ this technique.

In the past, it was customary to place the fiber in a solid metal block to which a groove in the shape of the letter V was cut. Impressive results

were achieved with this technique (2.5mJ, 5fs pulses at the output), however, the fiber‘s straightness was never perfect [6]. This has negatively impacted energy throughput.

Today this approach is considered outdated, as much better results are achieved with flexible stretched fibers. The fiber is made to be very flexible. It is then stretched between two anchors, providing a high degree of straightness. With this technique, the long-standing record of 5mJ, 5fs pulses has been surpassed and 6.1mJ, 3.8fs pulses were obtained [7], yielding more than TW peak power. In another experiment, 10mJ, and 10fs pulses were obtained using this technique [13].

Up until now, we have considered the pressure inside the capillary to be constant over the whole length. However, this may not be the optimal solution. A pressure gradient scheme has been successfully employed with great results. In this case, only the output of the fiber is pressured to a given value, and the input is kept in a vacuum. This creates a pressure gradient inside the fiber. Thanks to the very high resistance of the thin long fiber, the leaking of the gas through the capillary is usually no problem for the pumps on the vacuum side.

The advantage of this setup can be explained as follows. We know that at the input, the intensity is always higher than the output (due to losses). In a constant pressure setup, in order to not exceed the critical pressure and ionization threshold, the pressure has to be set according to the intensity at the fiber entrance. But this means that at the output, where the intensity is substantially lower, the broadening is much less efficient because the pressure could be much higher. This is solved by the pressure gradient.

Ionization is mostly seen as a parasitic effect that should be avoided at all costs. The reason is simple, it is linked with high losses, which are caused by the divergence of the beam that occurs during the ionization. Better results were generally achieved with higher pressure, at which the leading phenomenon is Kerr effect-induced SPM. This regime usually has higher throughput, achieving higher peak power at the output. The input pulses are usually slightly attenuated to suppress ionization in these experiments.

However, this does not need to be a concern with a sufficiently powerful laser. At some point, the input power becomes so high, that ionization is not avoidable anyway. If the energy is sufficiently high, even though losses may be significant, the output power can still be higher than in the case of SPM and weaker input pulses.

Indeed, ionization-induced spectral broadening has been successfully demonstrated on several occasions. [13] [14] [15]

Chapter 4

Experiment parameters

This chapter is devoted to assessing all parameters of the experiment. This includes identifying key limiting factors, which will determine the resulting form. The goal of this chapter is to produce concrete parameters like gas pressure, fiber length, and fiber inner diameter, which will then be used as a reference point for the design of the whole setup.

4.1 Limiting factors

As it was mentioned, the most important parameters are the gas pressure, fiber length, and fiber inner diameter.

4.1.1 Pressure

The gas pressure directly affects the achieved spectral broadening. For the case of SPM, higher gas pressure will result in more broadening, therefore it is desirable to increase the gas to the highest possible pressure. The limit here is the critical power, which is dependent on the pressure of the medium.

In the case of ionization broadening, the pressure affects the ionization dynamic, also changing the spectral broadening. Here the pressure must be high enough so that the change in refractive index is sufficient, but at the same time, it cannot be too high. Experiments show that at some point, saturation is reached and the spectra are not broadened anymore. Moreover, higher pressure leads to higher losses. [9]. Another side effect of higher pressure is creation of post-pulse in the recompressed pulse.

Helium will be used in both cases. For SPM, it is ideal thanks to its high ionization potential, and therefore high ionization threshold. In the case of ionization broadening, many rare gases were successfully employed in other experiments. While similar results are achievable with neon or argon [14], helium has performed the best. Its high ionization potential is once again an asset, as other rare gases get ionized too quickly in the strong laser field.

4.1.2 Inner diameter

The capillary inner diameter is linked with the ionization threshold. This parameter determines the beam radius, and therefore it affects the intensity. While thinner fiber will be able to provide higher B-integral through higher intensity (for SPM), we must be careful not to exceed the ionization threshold.

For the case of ionization broadening, intensity is the key parameter affecting the ionization dynamic. Too high intensity will result in rapid ionization during the first part of the pulse and the rest of the pulse is wasted. Too low intensity will on the other hand mean insufficient broadening.

4.1.3 Length

The capillary length is more of a practical limitation. Longer fiber will generally provide prolonged non-linear interaction, therefore producing a broader spectrum. Fiber as long as 6 meters has been successfully employed for post-compression, getting the highest average power few-cycle pulses to date [16]. The laboratory dimensions are often the factor determining the fiber length. We have to keep in mind that the beam is usually focused with large focal lengths. Moreover, when dealing with high peak powers, the last mirror has to be in substantial distance from the capillary.

4.2 Parameters for SPM

For convenience, we present once more parameters of the Legend laser in table 4.1.

Parameter	Legend
Pulse energy	12 mJ
Pulse duration	35 fs
Peak power	343 GW
Central wavelength	792 nm
Repetition rate	1 kHz

Table 4.1: Parameters of the Legend laser

4.2.1 Pressure

While the peak power of Legend is high, post-compression based on SPM (without ionization) has been achieved with sources of similar power [7]. The setup must be tuned in such a way, that critical power nor ionization threshold is exceeded. The critical power is given as

$$P_{crit} = \frac{0.148\lambda^2}{nn_2} \tag{4.1}$$

where n is classical refractive index and n_2 is the non-linear refractive index. Determining n_2 is not simple, as numerous models give quite different values. We shall use a model developed by Brée et al., which is in good agreement with experiments [17]. This paper gives the value of n_2 for helium equal to $0.37 \cdot 10^{-20} cm^2 W^{-1} bar^{-1}$. To give an example, the critical power for helium of atmospheric pressure, for a laser centered at $\lambda = 800\, nm$, would be roughly 241 GW.

If we take into account the actual power of the laser, we can easily see maximum pressure in the capillary if the collapse of the beam is to be avoided. This turns out to be roughly 0.7 bar. It should be noted that we have considered the pressure to be constant over the whole capillary. In reality, we will employ a pressure gradient scheme, as it was introduced in the previous chapter. Therefore the pressure at the fiber output shall be 1.5 times that, which is around 1 bar.

Another important remark is the fact, that while we have considered the critical power to be a fixed threshold, this does not have to be the case. The self-focusing dynamic becomes more complicated for ultra-short pulses on the femtosecond timescale, and it has been shown, that laser with higher-than-critical power can be used successfully for post-compression (employing the Kerr effect-based SPM) [18]. It may come to it that during the experiment, we shall increase the pressure at the fiber output beyond 1 bar, theoretically exceeding the critical power.

4.2.2 Inner diameter

The inner diameter is given by the ionization threshold. Should it be too small, the intensity of the pulse will become too high, and the gas will get ionized. This results in defocusing, loss of energy, and inferior beam quality.

As shown in chapter 2, the ionization dynamics is a complicated process. A sharp threshold cannot be determined, but we can make an educated guess and leave a margin for possible error. Based on multiple papers [19], [20], [21], we shall use the value $I_{th} = 3.62 \cdot 10^{14} W/cm^2$. Since the area of the fundamental mode propagating through the fiber is roughly half of the fiber core cross-section [22], we obtain the following equation for the diameter of the capillary:

$$a = \sqrt{\frac{2P_{peak}}{I_{th}\pi}} \tag{4.2}$$

Substituting for the constants into this equation, we obtain a maximum diameter of 492 microns. We will therefore round this value up and choose the fiber to have an inner diameter of 500 microns. While this doesn't guarantee complete suppression of ionization, it should mitigate it sufficiently.

4.2.3 Length

The fiber length will determine the interaction duration, which in turn will give us the spectral broadening. Overly long capillary will however have lower energy throughput, as well as more complicated and impractical installation and operation. The duration of a laser pulse produced by Legend is 35 fs. Two optical cycles centered at 800 nm are about 5.32 fs long. We can consider the necessary compression factor to be equal to 7. According to [23], the compression factor C is related to the B-integral as:

$$C = \sqrt{1 + \frac{4}{3\sqrt{3}} B^2} \tag{4.3}$$

Substituting for C, we get the value of B to be 8. Here we can exploit equation for B-integral which has already been introduced (2.15). In order for the equation to be valid, we need to consider homogenous pressure, minimal ionization, and the absence of self-focusing. Integrating equation 2.15 yields

$$B = k_0 n_2 I_0 \frac{1 - \exp(-\alpha L)}{\alpha} \tag{4.4}$$

where I_0 is the peak intensity, L is the medium length and α is the field atenuation constant of the EH_{11} mode. We are specifically considering this mode only, because for hollow core silica fiber, it is the least lossy one. Therefore, it is the only remaining mode at the output, all others are attenuated. The attenuation constant is according to [2] given as

$$\alpha = \frac{\lambda^2}{a^3} \frac{(\Delta n)^2 + 1}{2\sqrt{(\Delta n)^2 - 1}} \tag{4.5}$$

Here a is the fiber inner radius and Δn is the ratio of the refractive indexes of the fiber core and the cladding. Therefore we get the equation for the length of the fiber:

$$L = \frac{\ln\left(1 - \frac{B\alpha}{k_0 n_2 I_0}\right)}{-\alpha} \tag{4.6}$$

Substituting for all the constants we obtain the fiber length of 1.18 meters. To leave some margin for possible inaccuracies created by the many simplifications, we shall choose the fiber length to be 1.5 meters.

4.3 Parameters for ionization

We present parameters of L1:Allegra in table 4.2. Bearing in mind that it is a device still in development, we will take into account the current parameters as well as the parameters for which the laser is designed, so that the post-compression device remains functional as the input energy scales up.

Parameter	L1 (current)	L1 (designed)
Pulse energy	35 mJ	100 mJ
Pulse duration	15 fs	15 fs
Peak power	2.33 TW	6.67 TW
Central wavelength	825 nm	845 nm
Repetition rate	1 kHz	1kHz

Table 4.2: Parameters L1:Allegra

As we can see from the table 4.2, this laser is already far into the TW region, and the peak power will continue to increase. Post-compression of such a powerful laser, based solely on Kerr effect-induced SPM has not been demonstrated yet. Research has been done on this subject in [2], and while it is possible in theory, it is hard to imagine in practice.

The peak power is so high that if critical power is not to be exceeded, the gas pressure in the fiber would have to be very low. This would in turn dramatically decrease B-integral. To compensate for this and achieve sufficient spectral broadening, we would have to increase the fiber length significantly. The fiber would need to be over ten meters long. Just manufacturing such a long fiber would be a difficult task, and setting it up would be another challenge. Conditions in the E1 hall, where the experiment will take place, are not suitable for such a feat.

We shall therefore turn to ionization-induced SPM. While most articles support Kerr effect-induced SPM as the superior option thanks to its high energy throughput and excellent beam quality, good results have been achieved with the ionization scheme as well [13] [15].

Based on data from other similar experiments, it seems plausible that the fiber designed in the previous chapter could be used for ionization-based post-compression as well. This would give us a unique opportunity to operate the same device in two different regimes, employing completely different phenomena.

L1:Allegra has pulses with duration of 15 fs. It is better to leave some margin, as our calculations are not precise. Therefore we will aim for the compression factor to be 4.

We can write the frequency as a derivative of the phase:

$$\omega(t) = \omega_0 - \int_0^L \frac{\omega_0 z}{c} \frac{\partial}{\partial t} \left(1 - \frac{n_e(z,t)}{2n_c}\right) dz \tag{4.7}$$

Rewriting this equation will give us the following:

$$\Delta\omega \tilde{=} \frac{\omega_0}{c} \frac{\Delta n L}{t} \tag{4.8}$$

where t is the time, during which the change of refractive index occurs. Time-bandwidth product for a Gaussian pulse is given as:

$$\Delta f \cdot \tau = 0.44 \tag{4.9}$$

This gives us the necessary bandwidth of roughly 88 THz. Then we can rewrite the compressions factor as follows:

$$\frac{1}{4} = \frac{\Delta\omega}{\omega_0} = \frac{\Delta n L}{cT} \tag{4.10}$$

Here the refractive index is given as $n = \sqrt{1 - \frac{n_e}{n_c}}$. We can expand this formula into a Taylor series:

$$n = 1 - \frac{1}{2}\frac{n_e}{n_c} - \frac{1}{8}\left(\frac{n_e}{n_c}\right)^2 + ... \tag{4.11}$$

Let us suppose that the free electron density is at all times much smaller than the critical density. Then we can neglect higher terms and write:

$$n \tilde{=} 1 - \frac{1}{2}\frac{n_e}{n_c} \tag{4.12}$$

For non-ionized gas, the refractive index is obviously very close to 1. Therefore we can write $\Delta n = 1 - n$. Substituting this into the equation 4.12, we obtain

$$\Delta n \tilde{=} \frac{n_e}{2n_c} \tag{4.13}$$

Substituting this back into the equation 4.10, we obtain

$$n_e(100\%) = \frac{1}{2}\frac{n_c c t}{L} \tag{4.14}$$

Here $n_e(100\%)$ stands for free electron density when the whole medium is ionized. To calculate n_e when the whole gas is ionized, we can exploit the state equation for an ideal gas:

$$pV = nRT \tag{4.15}$$

Here p denotes pressure, V is volume, n is the amount of substance, T is thermodynamic temperature and R is the gas constant. To get the number of particles N into the equation, we use the relationship $N = n \cdot N_A$ where N_A is the Avogadro constant. And since $R = k_B \cdot N_A$ where k_B is Boltzman constant, we get the equation

$$\frac{N}{V} = \frac{p}{k_B \cdot T} \tag{4.16}$$

The number of particles divided by the volume is particle density, therefore if the whole medium is ionized, the free electron density will be given as

$$n_e(100\%) = \frac{p}{k_B T} \tag{4.17}$$

Therefore, we obtain the formula for gas pressure necessary to obtain the desired spectral broadening:

$$p = \frac{1}{2}\frac{n_e c t k_B T}{L} \tag{4.18}$$

We can estimate t to be roughly 5 femtoseconds. This does not need to be strictly accurate, as we can easily optimize the pressure during the experiment. Taking into account the capillary length $L = 1.5 \;\; m$, we obtain the necessary helium pressure around 8 mbar. This verifies the assumption that the same capillary can be used for ionization-induced SPM as well.

Moreover, the low pressure implies a low non-linear refractive index. Therefore we do not need to worry about exceeding critical power. The last validation that needs to be made is the one regarding neglecting the terms in the Taylor series. We can write the formula for critical pressure (the pressure of a medium, that of which 100 % ionization would result in reaching critical electron density): $p_c = n_c k_b T \tilde{=} 70.5$ bars. This is about ten thousand times higher than the actual pressure, therefore n_e will be much smaller than n_c and the assumption is correct.

Chapter 5

Simulations

In the previous chapter, we generated parameters of the experiment, that were based on many simplifications. In order to verify our assumptions and validate the parameters, we shall conduct simulations in Matlab, with the aim to show the induced spectral broadening.

The algorithm will be the same for both cases, the ionization and the SPM. The only difference will be the first step, in which the propagation itself is simulated. The goal of this step is to obtain the expression describing the pulse via the amplitude and phase in the temporal domain. In each of the two cases, a different method will be used to obtain this expression. Once we have it, we will apply the Fourier transform, obtaining the spectrum and spectral phase.

In the next step, we will fit the spectral phase by a second-order polynomial. This fitted parabola will then be subtracted from the spectral phase in order to simulate the compression on the chirped mirrors. The reasoning behind this step can be explained by bringing back Chapter 2, where it is shown that linear chirp (applied by the chirped mirrors) manifests as a quadratic spectral phase.

After subtracting the fitted parabola, we will be left with a quasi-flat spectral phase. This can be used to reconstruct the compressed pulse, which can then be inverse Fourier-transformed to get the temporal dependency. A diagram of the whole process can be found in image 5.1.

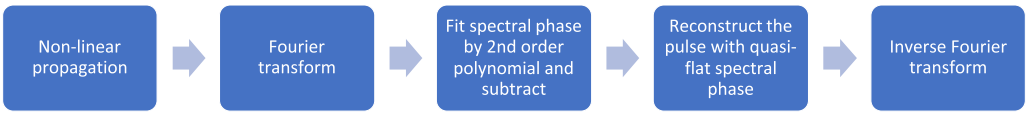

Figure 5.1: Simulation algorithm diagram

5.1 Ionization

As it was already mentioned, ionization is a complicated process, difficult to describe analytically. One possible approach for simulations is to solve the time-dependent Schrödinger equation (TDSE) for each individual atom. This is however tedious, complicated, and computation-heavy. The goal of this chapter is not to simulate precisely the process inside the capillary, but rather to provide us with a rough estimation. The approach of solving the TDSE is therefore not optimal.

Instead, we will use a theory has been developed by Keldysh [24], providing us with an expression for the probability of ionization of the atom in a strong EM wave. This work has been further improved, most notably by a trio of Ammosov, Delone, and Krainov (hence the so-called ADK model) [25]. We shall use another variant of this model, developed by Tong et al.[26]. This model is an extension of ADK, corrected for the barrier-suppression regime.

The ionization rate is given as:

$$W_{TBI} = \frac{C_l^2}{2^{|m|}|m|!}\frac{(2l+1)(l+|m|)!}{2(l-|m|)!}\frac{1}{\kappa^{2Z_c/\kappa-1}}\left(\frac{2\kappa^3}{F}\right)^{2Z_c/\kappa-|m|-1} e^{-2\kappa^3/3F} \quad (5.1)$$

Here l and m are angular momentum quantum numbers of the valence electron. C_l is the amplitude of the electron wavefunction in the tunneling region. Z_c is the effective Colomb charge, F is the field strength and κ is defined as $\kappa = \sqrt{2I_p}$, where I_p is ionization energy. Values of I_p and C_l for various gas atoms or molecules can be found in [8].

We know that $n(t) = \sqrt{1 - \frac{n_e}{n_c}}$ where n_e is free electron density and n_c is critical electron density. At the beginning, all atoms are neutral, therefore $n_e = 0$. After that, the density is rising until all particles are ionized. We can calculate the free electron density at that point according to equation 4.17.

To numerically calculate the time-dependent ratio of ionized particles q, we iterate as follows:

$$q(i) = q(i-1) + [1 - q(i-1)] \cdot W_{TBI} \cdot \Delta t \quad (5.2)$$

Since we are neglecting recombination, we simply add the particles generated in *i-th* step to those generated in step number $i-1$. Moreover, we add the factor $1 - q(i-1)$ to the number of particles generated in *i-th* step, to take into account atoms that were already ionized in the previous steps (we assume that each atom can be ionized only once).

To obtain the free electron density, we just need to multiply the ratio q by the free electron density for a fully ionized medium:

$$n_e(t) = q(t) \cdot n_e(100\%) \quad (5.3)$$

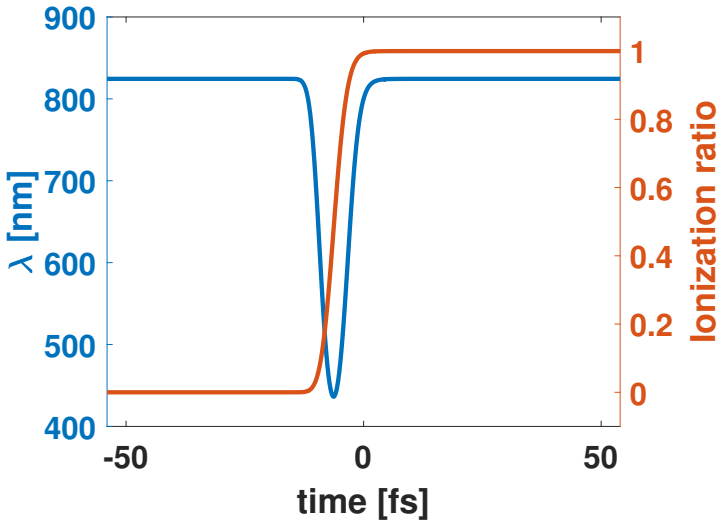

Figure 5.2: The evolution of the central wavelength of a pulse due to ionization of 8 mbar of helium

We simulate propagation through 8 millibars of helium. For simplicity, we assume the pulse to be pure Gaussian. The effective length of the capillary in the simulation is only 2.5 cm. This is because this simple model extremely overestimates the number of new frequencies generatedas it assumes the peak intensity through the whole propagation in the capillary. In reality, the intensity decreases considerably after first few cm of propagation. Shortening the effective length of the capillary aims to compensate for assuming other conditions to be ideal. The actual choice of the effective length is somewhat arbitrary, nevertheless, the chosen factor of 1/60 of the actual length should be conservative enough, taking into account experiences from other experiments [9]. The calculated ionization ratio together with the evolution of central wavelength is presented in figure 5.2.

Using equation the following equation:

$$\Phi(z,t) = \omega_0 t - \int_0^L \frac{\omega_0}{c} z n(z,t) dz \tag{5.4}$$

we obtain the pulse phase, which we can use to construct the whole pulse:

$$E = \exp\left(-1.38629 \cdot \frac{t^2}{\tau^2}\right) \cdot \exp(i\Phi) \tag{5.5}$$

We would like to know the duration of the pulse be if we manage to compress it optimally. By applying Fourier transformation we obtain intensity in the spectral domain. Spectral density and phase are shown in 5.3a. Here the spectral phase is shown after simulating the compression by subtracting the fitted second-order polynomial.

We can use this quasi-flat phase to reconstruct a new, compressed pulse. Then we can apply inverse Fourier transformation to get a temporal profile

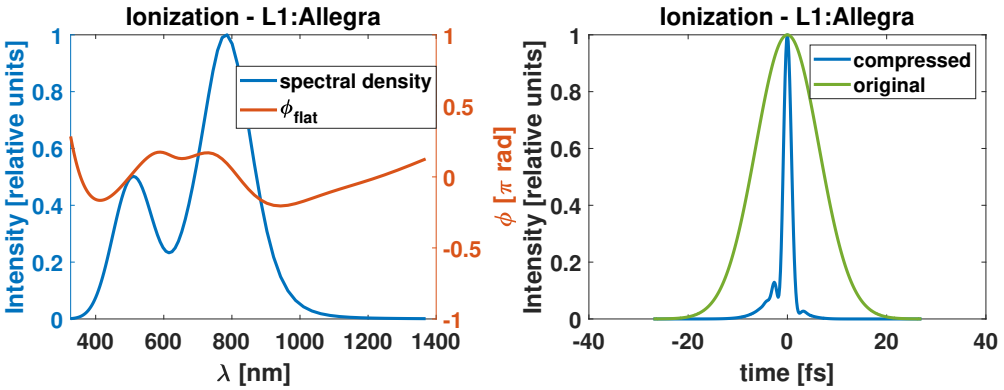

(a) Spectrum and phase of a recompressed pulse

(b) Original and recompressed pulse shape in temporal domain

Figure 5.3: Simulation of ionization induced broadening

of the new pulse. It is worth mentioning that the spectrum, as well as the temporal pulse shape, are not symmetrical. This is typical for ionization-induced broadening and it is caused by the fact that generated frequencies are proportional to the derivative of free electron density, which is a rising function. The spectrum is therefore strictly blue-shifted.

A comparison of the original and compressed pulse is shown in figure 5.3b. FWHM of the compressed pulse is 1.84 fs. Of course, we won't be able to achieve exactly this value, too many idealizations were made for that. However, we have verified that the designed parameters are reasonable for the L1:Allegra.

5.2 SPM

For the case of Kerr effect-induced self-phase modulation, the simulation will be simpler, as getting the temporal dependence of the refractive index is more straightforward. It is given as

$$n(z,t) = n_0 + n_2 \frac{I(z,t)}{2n_0\epsilon_0 c} \tag{5.6}$$

Through the equation

$$\Phi(z,t) = \omega_0 t - \frac{\omega_0}{c}\left(n_0 + n_2 \frac{I(z,t)}{2n_0\epsilon_0 c}\right) z \tag{5.7}$$

we obtain the phase accumulated during the propagation through the capillary. The equation 5.5 gives us the pulse in the temporal domain. From here the simulation continues the same way as in the previous case. The results are presented in the following figures.

We should notice that in this case, the spectrum is symmetrical (in ω). This is typical for SPM and it is given by the symmetrical shape of the pulse.

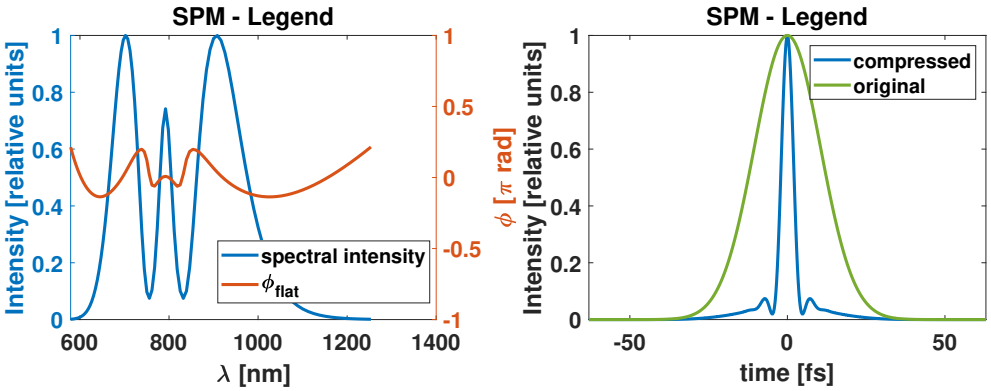

(a) Spectrum and phase of a recompressed pulse

(b) Original and recompressed pulse shape in temporal domain

Figure 5.4: Simulation of SPM induced broadening

Chapter 6

Design implementation

Three versions of the experimental setup were developed. The first version considers all aspects of the experiment and it is supposed to serve as a base for future development of the device.

However the full experiment is too extensive and cannot be completed within a single Master's thesis. Thus the practical part of this work will focus solely on ionization-induced spectral broadening using L1:Allegra as the source laser.

The second version of the design implementation will hence describe the setup used for ionization-induced spectral broadening only. It will not include the compression stage. Another difference from the complete version is that it will include old vacuum chambers that are currently present in the E1 experimental hall. These will not be sufficient for the full experiment as there is not enough space for the compression stage, and they will be replaced in the future.

A force majeure intervention has forced us to develop a third model. At the end of March 2023, just a few weeks before our allotted time on the L1:Allegra laser, ELI Beamlines became a target of a cyber attack that has paralyzed its network and most of its control systems. Unfortunately, L1:Allegra was temporarily put out of service and it wouldn't be operational in time. Therefore we were forced to use an alternative source, a less powerful tabletop laser system which was present in the E1 hall. Small adjustments were made to make the original setup compatible with the new laser source.

6.1 Complete experiment

A complete research of implementation of the experiment was conducted. The most restricting criterion is free space in the experimental hall. It is already relatively crowded and other experimental setups that are present need to be considered. The layout of the hall in the current state before the experiment can be found in image 6.1. In the future, additional chamber will be placed between chambers 10 and 11, and the current chamber 12 will be

exchanged for a bigger one.

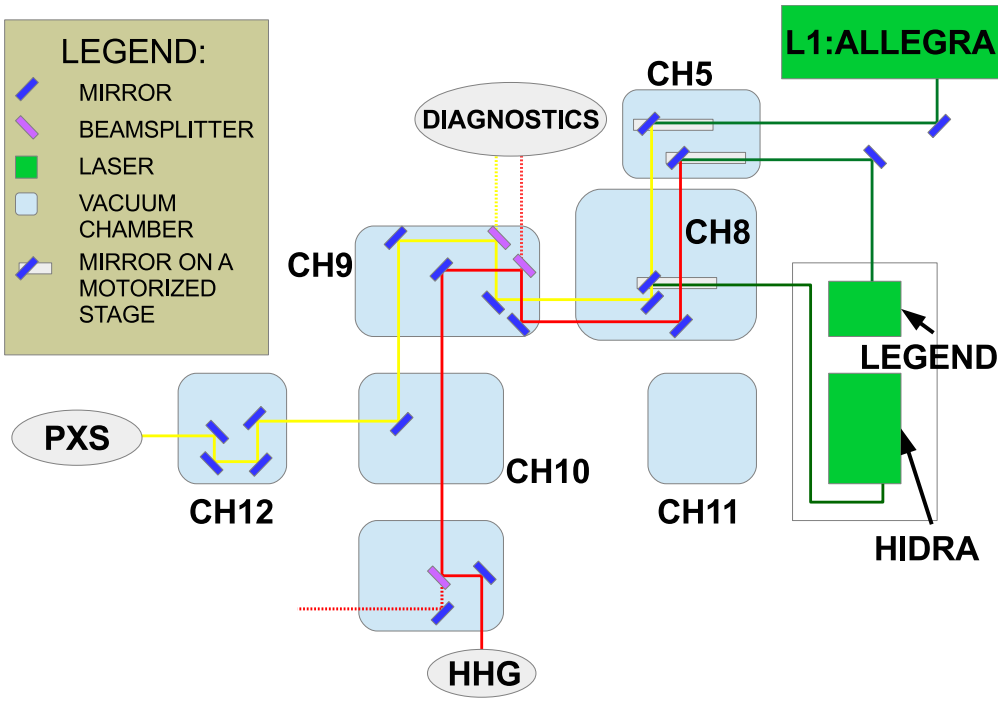

Figure 6.1: Simplified layout of the E1 hall before the experiment

Alloted space is in chambers 10, 11, and 12. Furthermore, parts of chambers 10 and 12 should be left empty, as the space will be required for other experiments. This factor already constricts the setup by a large amount.

First, we need to determine the focusing distance, because it determines the beam convergence angle. This in turn governs the focus size through the beam parameter product (BPP):

$$BPP = w_0\theta = \frac{\lambda}{\pi}M^2 \tag{6.1}$$

where w_0 is the beam waist radius, θ is the divergence (or convergence) half-angle, λ is the laser central wavelength and M^2 is a factor defining the beam quality. Perfect Gaussian beam has $M^2 = 1$, any real beam has $M^2 > 1$. We know that the fiber inner diameter is 500 µm, and that the beam diameter (measured at e^{-2} should be 0.69 times that to ensure ideal coupling. This means that the beam waist should be 172.5 µm (radius at e^{-2}), which gives us the convergence half angle of 1.48 mrad.

Because the waist of a collimated expanded beam of L1:Allegra is roughly 30 mm, the focal length of the focusing mirror should be around 10.5 meters. This is another large restriction. Because of the high intensities that we are dealing with, the last mirror should not be closer to the focus than 4 meters, otherwise we risk damaging the mirror.

There are three options for achieving the desired focus size. The most obvious one is to use a single spherical mirror of the given focal length. The main advantages of this option are simplicity, compactness, and the fact that only a single curved mirror is required.

The second option is to use a telescope. This way some space can potentially be saved, as the actual focus distance is shorter than the effective one. More importantly, it can be used to correct aberrations like astigmatism. On the other hand, this requires precise angles between the mirrors, which may potentially require additional space inside the chambers. This option is generally less versatile and more finicky.

The third option is to reduce the size of the beam first by parabolic telescope, and then use a mirror with a shorter focal length. Again, some space can be potentially saved, as the actual focal length decreases. But the parabolic mirrors are very sensitive to precise alignment, otherwise, aberrations occur.

One factor that has not been mentioned yet is the fact, that the collimation of the source laser may fluctuate. As the device is still in development, changes are made regularly. This results in change of some of the laser parameters, collimation included. Therefore the focal spot may shift by as much as a few tens of centimeters. We need to be able to react to this kind of change.

Research comparing all three options was conducted in Zemax and the results were compared to another study made in Inventor. The research in Inventor has quickly revealed that using a parabolic telescope is not efficient. The space saved by the shrinkage of the beam size is outweighed by the space taken up by the parabolic mirrors themselves. Moreover, it adds unnecessary complexity, so there is no reason to consider this solution any further.

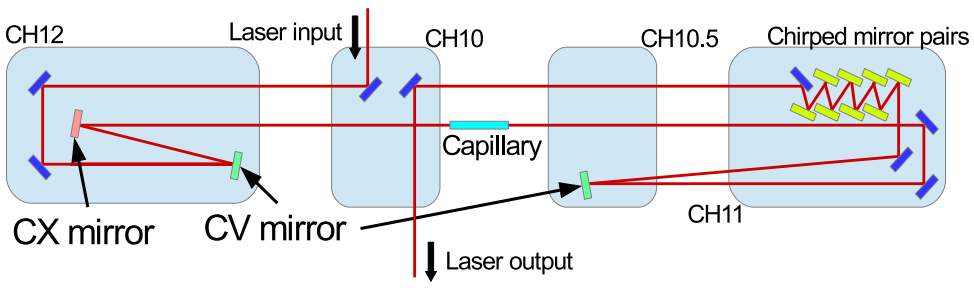

Figure 6.2: Diagram of the setup for the full experiment, telescope version. CX denotes convex, CV denotes concave, CH denotes chamber. The whole setup is under vacuum, tubes are not depicted in the diagram.

The telescope variant and the single curved mirror variant were both feasible. The main benefit of the telescope is its ability to correct astigmatism, to which the fiber is highly sensitive. On the other hand, it would take up considerably more space and, more importantly, its ability to react to changes

in the beam collimation is severely limited. As precise distances and angles between the mirrors need to be maintained, with two given mirrors we would be able to react to only small changes by moving the mirrors on motorized stages. For bigger changes, the mirrors would have to be swapped and the whole setup rebuild, as different focal length of the mirrors will change all the other parameters as well. To be able to react sufficiently, about 6 different concave mirrors and other 6 convex mirrors might be required. While the prospect of an aberration-free beam is attractive, the complexity is just too high. The diagram of this variant is in image 6.2.

For this reason, we decided to implement the variant with a single concave spherical mirror. This variant is charmingly simple, as seen in diagram 6.3. One of the surprises came from the Zemax analysis. Given the small angles, there are almost no aberrations introduced by the spherical mirror. The Zernike polynomial with the highest coefficient is astigmatism, its coefficient being only $4 \cdot 10^{-3}$. We will be able to react to major changes in beam collimation by simply translating one of the planar mirrors on a motorized stage. Swapping mirrors should not be required, saved for the most pronounced changes in collimation. We won't be able to correct any aberrations that might be present from before, but hopefully, this will not be a major issue.

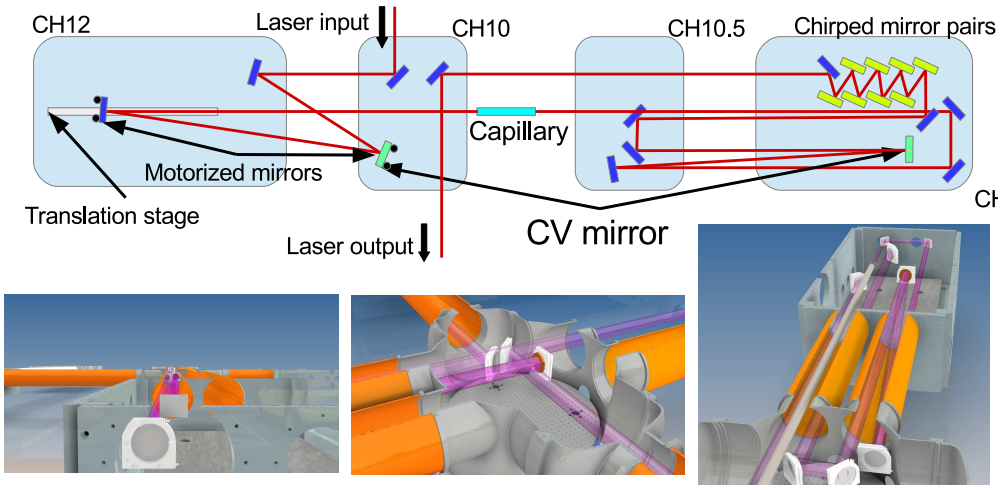

Figure 6.3: Diagram of the setup for the full experiment, single focusing mirror version. Snapshots of respective parts of 3D model. CV denotes concave, CH denotes chamber.

A complete 3D model of the chosen variant was developed. This model includes all mirrors on both sides of the capillary, the fiber itself, and parts of the vacuum system. It will serve as documentation for further development and use of the device.

6.2 Setup for practical part

The goal is to build a focusing setup that would enable optimal coupling into the fiber, and then build the vacuum apparatus behind the capillary. Behind the output window, a spectrum will be measured to verify the achieved spectral broadening.

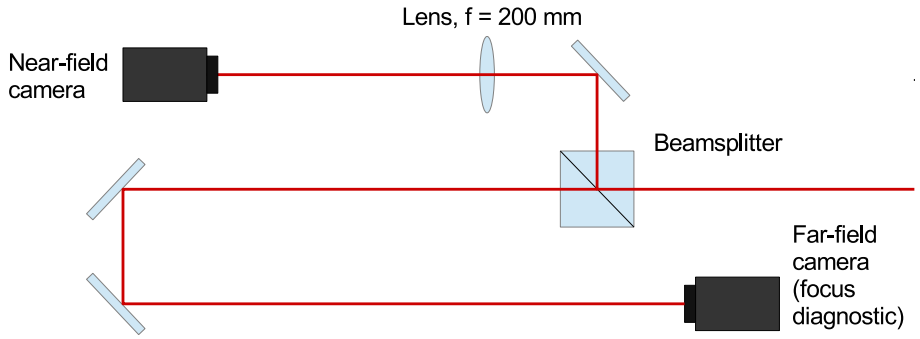

(a) Diagram of diagnostic

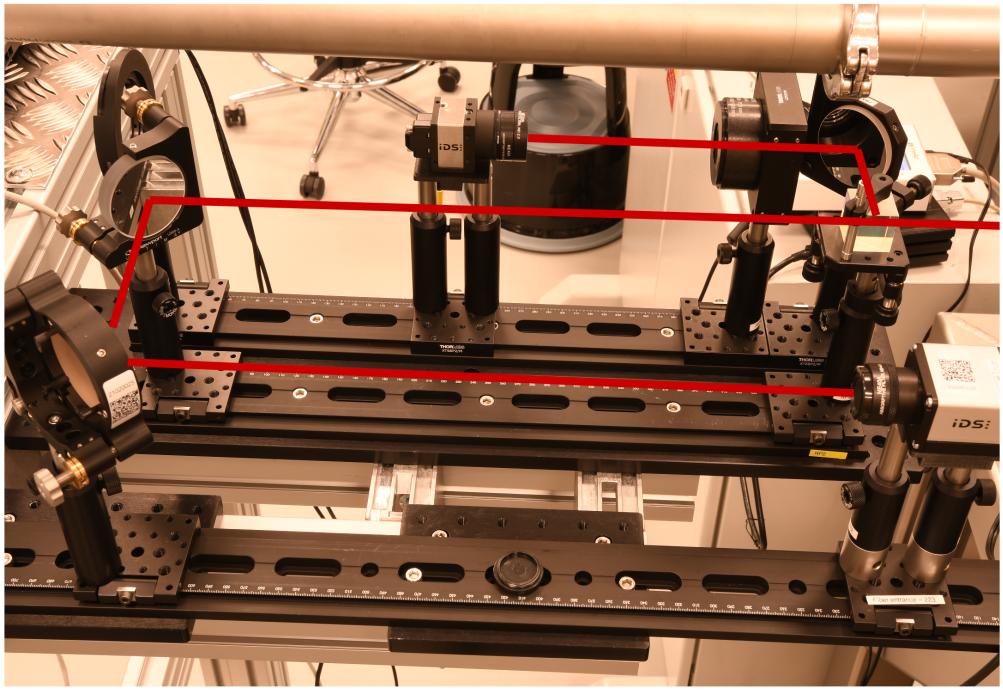

(b) Laser path added as a drawing for clarity

Figure 6.4: Designed diagnostic setup

The focusing setup is mostly identical to the one outlined in the previous section, but with a different chamber 12 and with absent chamber 10.5. Current chamber 12 is connected to chamber 10 via a single channel and it has

different dimensions. Moreover, it is already partly filled with mirrors used by a different experiment. Both of these facts meant that minor adjustments were required. The capillary was moved to a different location and slightly different vacuum system was designed.

An integral part of the setup is beam diagnostic. Diagram of the designed setup can be found in figure 6.4. For the coupling efficiency, a perfect beam alignment with the fiber is curcial. Fluctuations of the beam pointing need to be corrected for. To achieve this, the following setup was built. In chamber 10, a pellicle beam splitter inserted into the focused beam. This reflects about 8 % in the downward direction, towards the breadboard. A fused silica wedge is placed here at an angle of 45°, reflecting roughly 1 %. The wedge fullfills the role of slightly reflective surface, while preventing any back reflections and ensued interference. From here the beam propagates in parallel to the original beam to a cube beam-splitter.

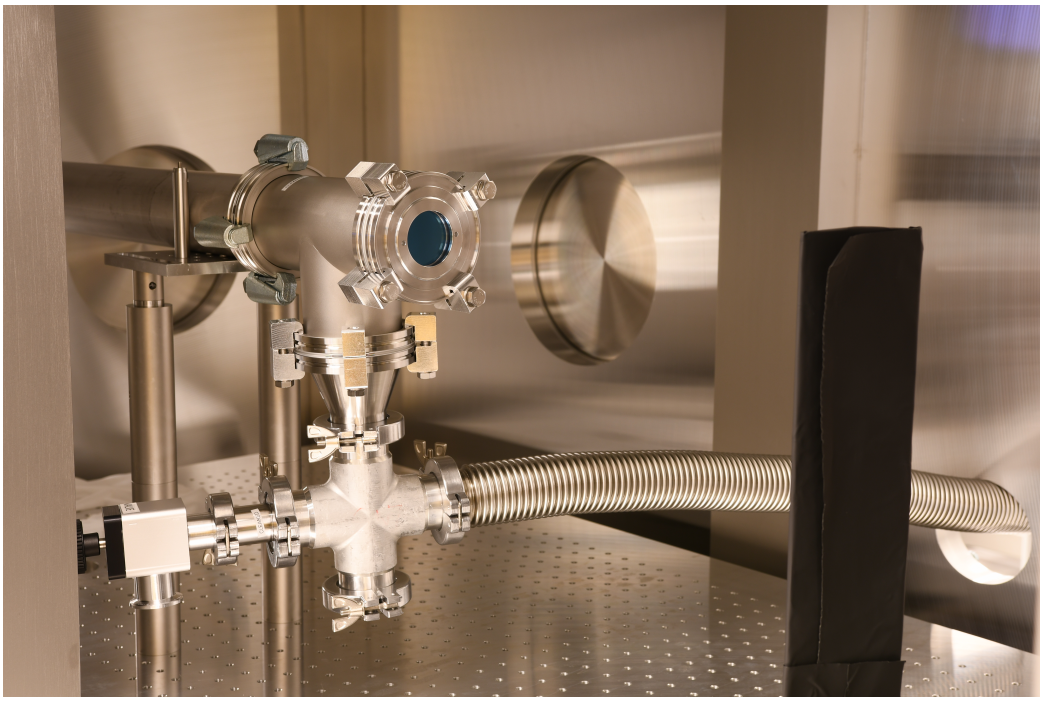

Figure 6.5: Gas tubing with output window. To regulate the pressure in this section, a venting valve and a scroll pump were installed.

One part is sent directly to a camera placed at the exact same distance from the pellicle as the fiber entrance. This part of the diagnostic is referred to as the far field and it serves two purposes. First, it helps to determine the size of the focus. The camera can be translated in the z direction in order to scan for the exact focal point, which can then be adjusted to coincide with the fiber entrance. The second purpose is to serve as a first reference for a perfectly aligned beam.

The second part of the beam is sent from the beamsplitter cube to a 200 mm lens, projecting an image of the last mirror onto the camera. This part

of the diagnostics is referred to as the near field, and it serves as the second reference of the perfectly aligned beam. In order to place the camera exactly in the image plane, the lights in the hall must be turned off and a powerful LED must be shone on the imaged mirror. Only then the image is visible on the camera and sharpness can be verified.

When the setup is at atmospheric pressure and the vacuum tubing is removed, we can align the beam at the input and the output fiber holder, checking the position of the beam by the naked eye. The alignment is provided by the spherical mirror and the last (planar) mirror. Once the alignment is complete, the references on the cameras are noted. Once the system is put under vacuum, alignment must be doable solely with the cameras. The alignment mirrors are motorized, therefore we can align the beam to the saved references according to the diagnostic cameras.

The cameras also give us other general information about the beam, for example, the beam shape, fluctuation of the beam position, focus size and focus position, presence of astigmatism, etc.

A vacuum tubing, 4 meters in length, was installed at the output of the capillary. This tubing featured a window at its end, which was used to direct the beam towards a 50:50 beamsplitter cube located behind it. Here, a camera and energy meter were placed to capture and measure the beam. To further analyze the beam, a sheet of paper was used to reflect some of the light into a spectrometer. This section of the setup was specifically designed for characterizing the beam at the output of the fiber, and more detailed information will be provided in the next section. A photograph of the output side, featuring the window, can be found in Figure 6.5.

Chapter 7

Experimental data

This chapter is devoted to the experiment itself. The goal was to use L1:Allegra for ionization and measure the spectrum. This was intended as a proof of concept, to show that everything is working as intended and sufficient spectral broadening is achieved. Should we succeed, a compressor based on chirped mirrors would be built, completing the device.

Unfortunately, a force Majeure intervention prevented us from realizing this plan. In the weeks preceding the experiment, when we were building the setup, ELI Beamlines suffered a cyber attack which has paralyzed the facility network and temporarily put out of use most of the control systems, involving L1:Allegra.

There are two other lasers available in the E1 hall. One of them, Legend, has been introduced already. Its peak power is not high enough for ionization broadening. The post-compression would have to run in the Kerr effect regime, however, that would probably require overpressure in the system. The setup was not prepared for that yet, and there was no way to modify it in time.

Parameter	Hidra
Pulse energy	50 mJ
Pulse duration	90 fs
Peak power	555 GW
Central wavelength	800 nm
Repetition rate	10 Hz

Table 7.1: Parameters of the Hidra laser

Therefore we decided to use the third laser, Hidra. This is, like Legend, a commercial device manufactured by Coherent. While the amplifier provides 100mJ pulses, due to the size of the compressor half of the energy is dumped. The overview of specifications can be found in table 7.1.

The pulse duration is significantly higher then what is given by the manufacturer. The laser is under construction, currently operating with a tempo-

rary solution of the compressor and beam expander. Currently, it is realized via a lens telescope. The nonlinear processes occurring in the glass lenses are the cause of the longer pulses. Moreover, they negatively affect the beam profile. The lens telescope is being replaced by a mirror one, however, this is work in progress. The peak power is anyway higher than that of the Legend laser.

A variable attenuator based on Brewster reflection is installed between the amplifier and the compressor. This allows for continuous output power tuning.

Given the different laser source, we decided to use argon instead of helium. With Hidra, it would be difficult to ionize the helium fast enough to high enough levels. Argon has a lower ionization potential and it will get ionized much faster. To adjust for the different gas, the pressure has to be changed as well. We expect the optimal pressure to be in tens of mbar, optimal value will be found during the experiment.

7.1 Alignment

The setup is built according to the plan presented in the previous chapter. The optical elements are placed with the help of a total station, with a deviation <0.5 mm from their respective positions given by the 3D model.

Special attention needs to be paid when installing the vacuum tubing. The tubes need to line up perfectly with the capillary mounts, otherwise, the leverage forces pulling on the mounts will ruin the fine and delicate capillary alignment. Bellows are inserted on each side between the capillary mount and the tubing, to further mitigate any remaining leverage force.

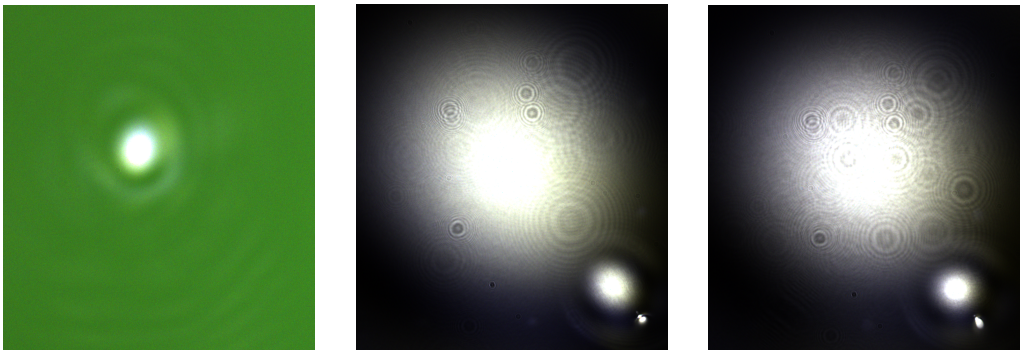

(a) Beam during alignment, directly at fiber output

(b) Alignment under vacuum, E = 200 µJ, p = 0 mbar

(c) Beam during experiment, E = 5.8 mJ, p = 50 mbar

Figure 7.1: Beam shapes as seen on camera at the output of the capillary after alignment. Image (a) is directly behind fiber. Images (b) and (c) are behind the output window, where lens was required. The small spots in the corner are artifacts caused by reflections from ND filters

After the setup is built, preliminary alignment of the laser beam needs to be done. This is done with the fiber removed from the setup. The spherical focusing motorized mirror is used for alignment at the input capillary holder, while the flat motorized mirror aims at the output holder. When this is done, the laser is blocked and the capillary is inserted.

The next step is to stretch the fiber. This assures its perfect straightness. In total, the fiber is stretched by about 1 millimeter. First, the tip/tilt screws are adjusted so that the fiber is centered with respect to the holders on both sides. After that, the straightness of the fiber is adjusted. It is tightened until it looks straight to the naked eye. Then a washer is placed on top of a post and both are placed under the fiber directly at the output holder. The height of the post is adjusted so that the washer almost touches the fiber and no gap is visible between the two. The post with the washer is then placed in the middle of the fiber. If the fiber sags, it will push on the washer when the post is slid underneath it. The fiber is then stretched until no contact between the fiber and the washer is noticeable anymore. Figure 7.2 shows fully set up fiber in the E1 hall.

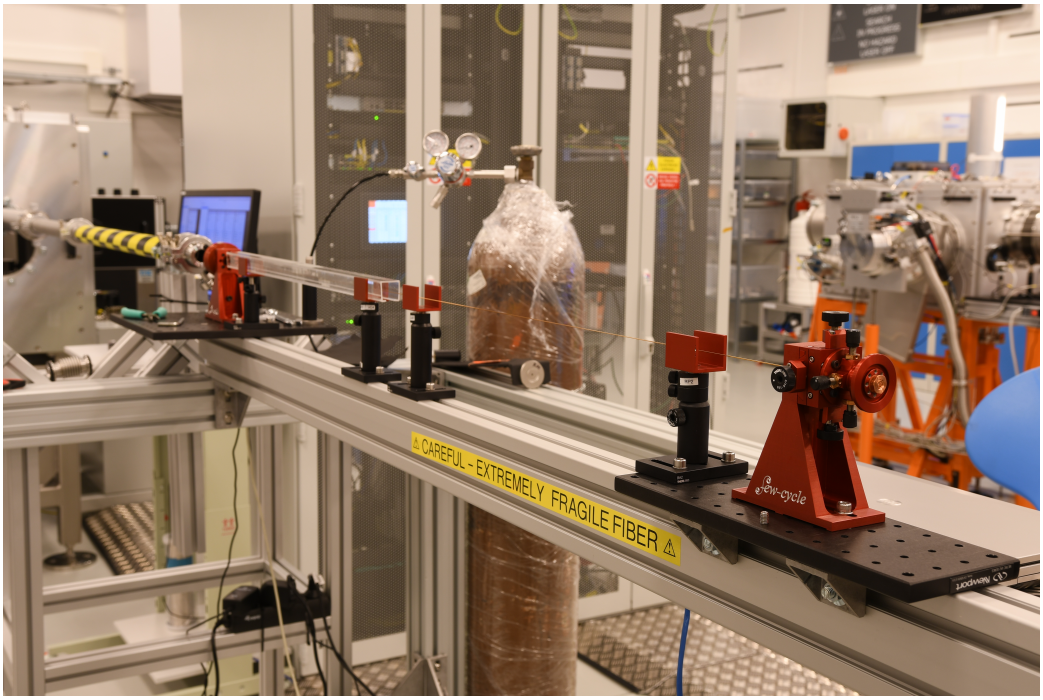

Figure 7.2: Fully set up fiber in the E1 hall (before finishing installation of the vacuum tubing)

After stretching the fiber, the laser can be turned on on the lowest power setting, and the beam can be sent to the fiber. The beam is now visible at the output of the fiber as well. The next alignment is done with a power meter and a camera both placed at the fiber output, behind a beamsplitter. The fiber alignment consists of four elements: an x/y translation stage at the input, tip/tilt screws at both the input and the output and finally a z

translation stage at the output for stretching the fiber. The tip/tilt axes at the input and output are crossed, making a 45° angle. The fiber alignment algorithm is as follows:

1. The x/y stage is optimized. This mostly affects the energy throughput, but usually doesn't have a noticeable effect on the output beam shape.

2. Output tip/tilt is optimized. The beam at the output usually comprises 2 central disks (often distorted), surrounded by Airy rings (also often distorted). Each of the two tip/tilt adjustments mainly affects only one of the two disks, the input and output alignment is mostly decoupled. The goal is to join the two disks and eliminate any distortions and asymmetries.

3. The x/y stage is optimized again. It is important not to skip this step.

4. Input tip/tilt is optimized. This is done in the same way as the output side but with the second disk being affected. The tip/tilt alignment is governed mainly by the beam shape, however, energy throughput also plays a role.

5. The x/y stage is optimized again.

6. Steps 1-5 are repeated until no further progress can be made. Only then the fiber can be stretched by another half-turn. After stretching the fiber, another iteration of steps 1-5 needs to be made. In total, the fiber can be stretched by 1-2 turns maximum from the point when straightness was first verified with the post and washer.

After the fiber was completely aligned and no more progress could be made, retaining rings were put in place and the vacuum tubing was installed. After installing the tubing, alignment was checked, as there still was some leveraging force remaining which slightly pushed on the fiber. Only then the setup was complete and the measurement could begin.

Illustrative images of beam shapes after propagation through well-aligned fiber can be found in image 7.1. The green tint in the first picture is caused by the gain of the camera, which was tuned as filters were being added. Because the camera was directly at the fiber output where the intensity was very high, we were being careful not to destroy the chip, hence we added many neutral-density filters for redundancy. Consequently, the gain had to be raised resulting in the green hue.

The two images on the right were taken when the setup was under vacuum and the camera had to be placed behind the output window. Here the beam was much larger because the window was placed roughly 4 meters from the fiber output to mitigate non-linearities and avoid laser-induced damage. In order to fit onto the camera chip, a lens was required. Multiple absorbive ND filters were used here as well. Reflections from these filters were causing

the multiple spots which can be seen in the images. Because of the added lens, in this case, the beam was converging. Even though most of the energy was lost as the reflectivity of the filters is low, the spots are visible due to the higher intensity.

7.2 Data measured with Hidra

Before putting the whole setup under a vacuum, we measured the throughput of the beam transport. It appears that around 1/3 of the energy is lost between the laser end and the fiber input. This shall serve as a benchmark for future measurements, where the pulse energy can be measured only directly at the laser output (before entering the vacuumed beam transport). We have neglected losses due to the atmosphere, as the intensity in the fully expanded beam is not high enough to have an impact.

7.2.1 Effect of intensity

Throughout the experiment, we had to adjust the Hidra compressor in order to achieve the shortest possible pulses with the highest possible intensity. It is important to remember that the shortest pulse at the laser output doesn't automatically mean the shortest pulse at the capillary input. Because of the high intensity, dispersion in the telescope and in the beam transport entrance window is not negligible. Therefore we compared all compressor adjustments with changes in spectrum and energy at the capillary output.

It was also necessary to adjust the fiber according to the fiber alignment algorithm that was described before, because of fluctuations in the laser beam pointing.

7.2.2 Effect of pressure

The pressure varied between 0 and 50 mbar. With pressures below 30 mbar, practically no broadening was noticeable. Over this value, the spectra began to broaden noticeably towards the short wavelengths. At 50 mbar the broadening was clearly visible. Near the edge of the spectrum (770 nm), the increase in counts against empty fiber was by 46 %. Further in the blue direction, at 765 nm, the increase was over 100 %. In empty fiber, there were hardly any counts (save for noise) below 750 nm. This threshold has shifted in the presence of Argon to 730 nm. The graphs describing the spectra are in picture 7.3.

7.2.3 Effect of input iris size

In the other part of the experiment, we measured the spectra with respect to input iris size changes. Firstly, the iris diameter governs the energy throughput. This was the most significant factor. Moreover, the iris size crops the

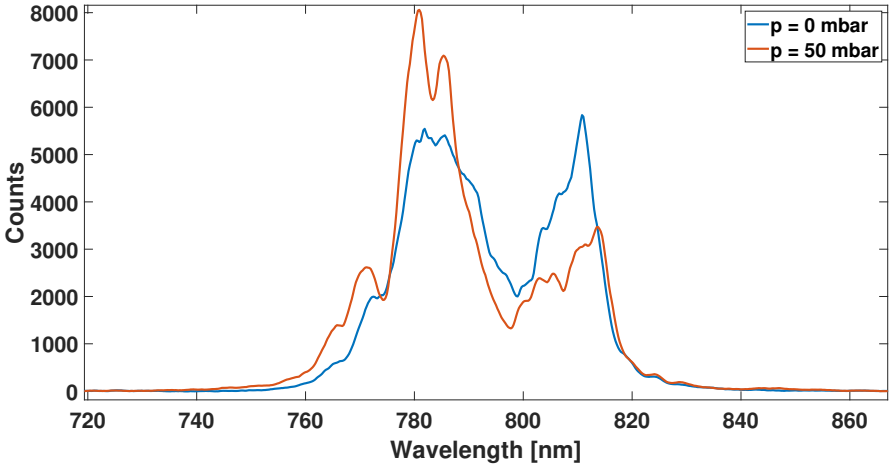

Figure 7.3: Hidra - Achieved spectral broadening

beam, effectively decreasing the convergence angle, therefore the focus increases in size. This affects the coupling into the fiber. Third, the decreased iris size improves beam quality, as it essentially acts as a spatial filter. The smaller the iris, the closer it is to a point source. A cleaner beam will be able to couple more efficiently. The measured spectra are in image 7.4.

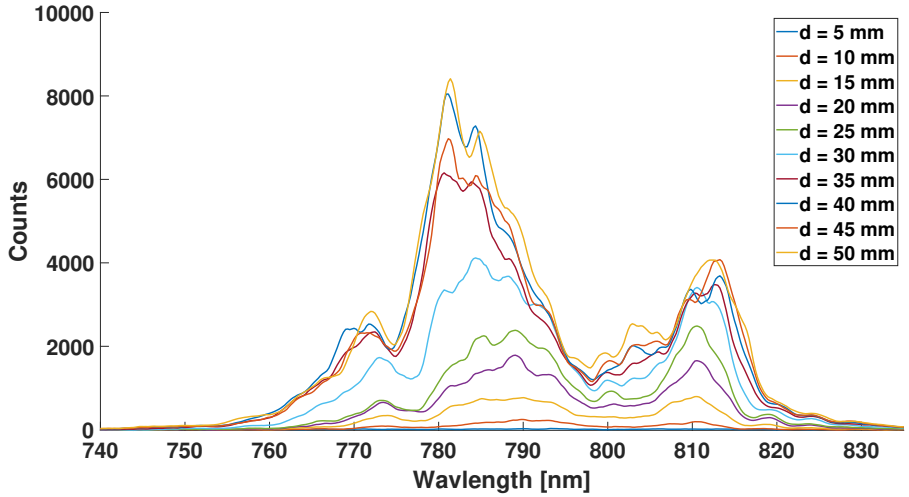

Figure 7.4: Hidra - Spectra vs. input iris size. Peaks become progressively more blue-shifted.

Complementary to this graph is the dependence of energy throughput with respect to the iris diameter. It can be found in image 7.5.

In the spectra in image 7.4, we can see a threshold at the iris size of 30 mm. This responds to an output pulse energy of 3.2 mJ. Input energy cannot be estimated, because the beam profile at the iris is far from Gaussian. At this point, the spectrum broadens visibly beyond 760 nm. This can be due

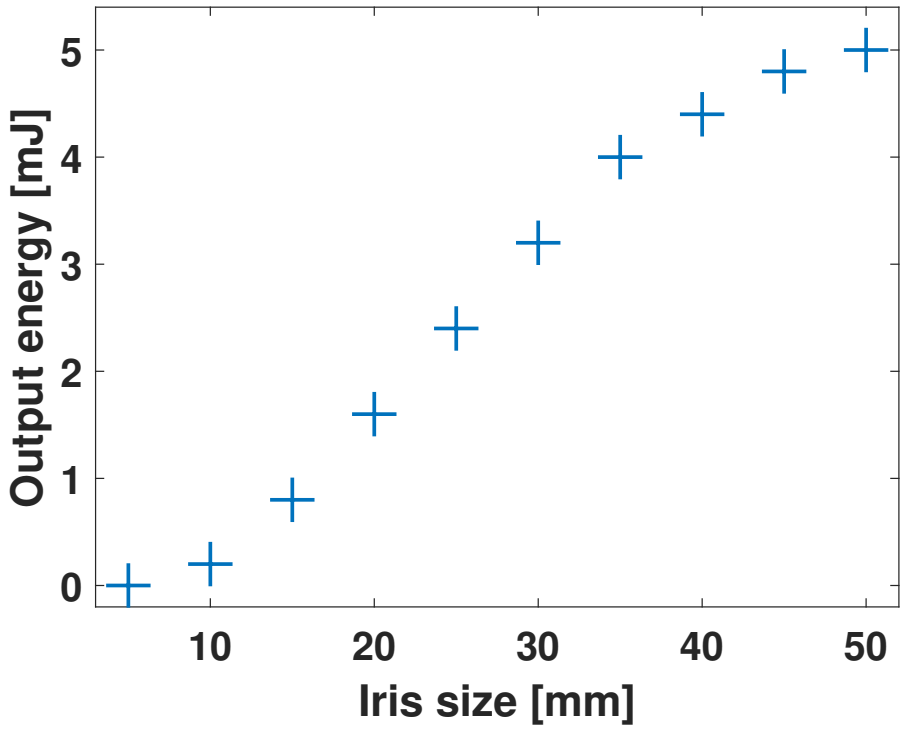

Figure 7.5: Hidra - Energy at the fiber output with respect to the entrance iris size.

to two factors. Either the input energy became high enough, or the focus became small enough for sufficient coupling. Probably it is the combination of the two. At the next step, the spectra are shifted even further (probably due to higher energy input), but for the remaining steps, they remain rather similar.

One might notice that for the iris diameter of 45 mm, the intensity suddenly drops. This cannot be caused by beam quality being worse than in the previous step or by the focus being too small, because this would only get more pronounced in the next step. However, at 50 mm the spectrum is almost the same as it was at 40 mm. Moreover, at this iris diameter, there is hardly any cropping present. This will thus most likely be caused by laser fluctuation.

7.2.4 Energy throughput

During the alignment, the input energy was 470 µJ, and the energy at the output of perfectly aligned fiber was 104 µJ, giving transmission of about 22 %. At the maximal intensity, however, the input energy was around 32 mJ and the output energy was 6 mJ at most. The transmission decreases below 19 %. The most plausible explanation is that due to non-linear effects in the telescope, at higher intensities the beam quality has worsened, impairing

the coupling. The effect of gas in the capillary was measurable but minor. Without any gas, the maximum throughput was 6 mJ, while with 50 mbar of argon, it was 5.8 mJ.

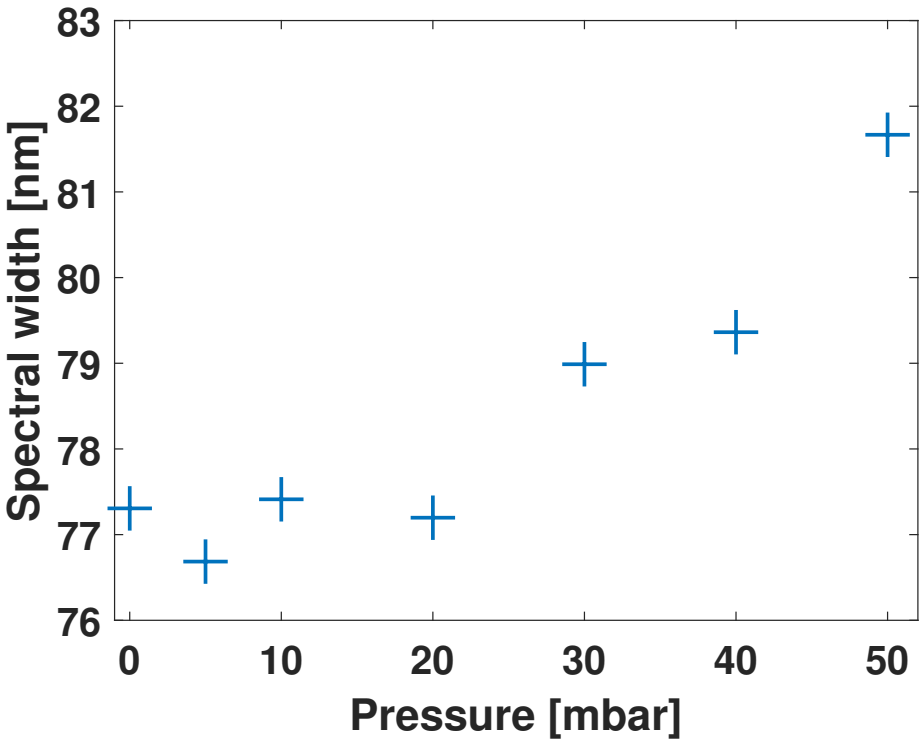

Figure 7.6: Hidra - Bandwidth (at e^{-2} with respect to pressure inside the capillary

7.3 Data measured with L1:Allegra

In the end, we were able to use L1:Allegra for measurements as well. Only 4 amplifier stages were available, providing roughly 4 mJ pulses at the laser front end. Pressure control was limited, as the device used for this purpose in the previous experiment broke down. The pressure was controlled via a needle valve, but there was no way to measure its value at the fiber output.

We pressurized the output side until significant broadening was present. Then we slowly decreased the pressure with a scroll pump, recording the spectra in the process. This was done until no broadening was present. The evolution of bandwidth based on pressure is presented in figure 7.7.

The broadening is mostly ionization induced, the spectrum is extended as far as 600 nm, compared to 750 nm without any gas present. Nonetheless, the gas pressure was high enough that increase in counts is noticeable in longer wavelengths as well, implying some amount of Kerr effect. The prevailing

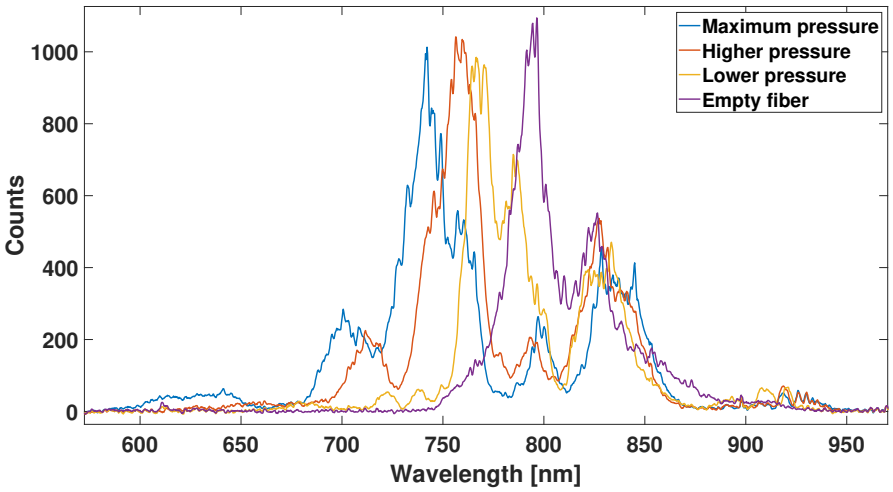

Figure 7.7: L1:Allegra - Spectra with respect to relative gas pressure

ionization nature of the broadening is, however, confirmed by the evolution of the central wavelength, as presented in figure 7.8.

The broadening cannot be quantified simply by measuring the bandwidth at a given value. The chosen value can completely change the result because of the rough shapes of the spectra. It is better to use integral method. Evolution of the spectral width in the form of RMS is presented in figure 7.8, together with the evolution of central wavelength.

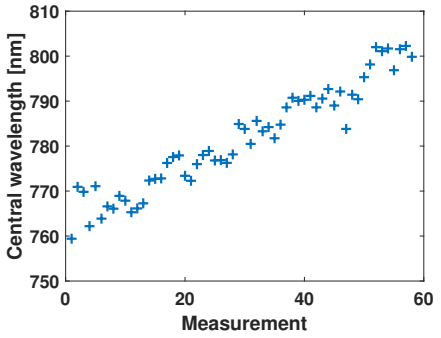

(a) Central wavelength evolution with respect to changes in gas pressure

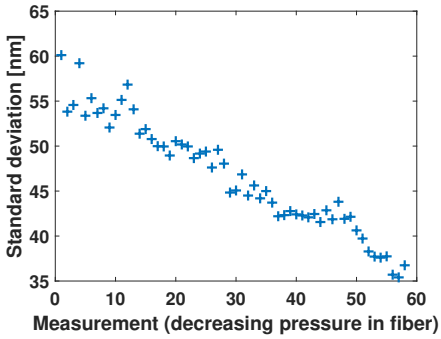

(b) Bandwidth (standard deviation) evolution with respect to changes in gas pressure

Figure 7.8: L1:Allegra - statistic of the measured spectra. Gas pressure gradually decreased throughout the measurement. Bandwidth presented in integral form.

7.4 Results

To summarize, in the first part of the experiment, we have achieved spectral broadening in 50 mbar of argon, due to ionization-induced self-phase modulation. The input pulse energy was roughly 32 mJ and the output pulse energy was 6 mJ, giving the transmission of 18.7 % in the fundamental mode.

When we were increasing argon pressure in the fiber, the spectrum was getting progressively wider. This can be seen in image 7.6, where the dependency of bandwidth on pressure is presented. The broadening is very small because the coupling of the beam is suboptimal and the pulse peak power is low to begin with. Nevertheless, it shows that ionization-induced broadening is present.

In the second part, the pulses were supplied by L1:Allegra. We have shown significant ionization-induced spectral broadening with traces of Kerr effect-induced spectral broadening. In the presence of gas, the central wavelength has shifted from 800 nm to 760 nm. The bandwidth has almost doubled. Total evolution of spectra over the whole measurment with L1:Allegra can be seen in figure 7.9.

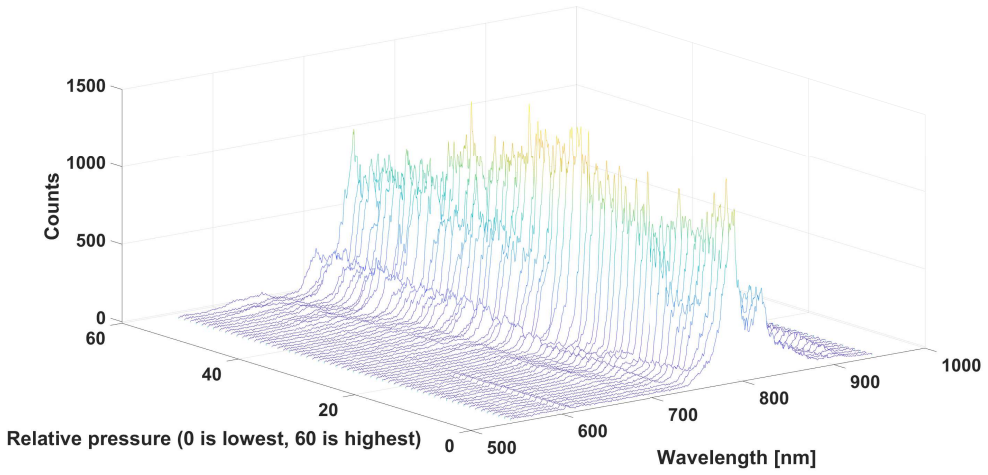

Figure 7.9: L1:Allegra - Total evolution of spectra with respect to relative gas pressure

Chapter 8

Conclusion

The objective of this thesis was to investigate the post-compression of high-power femtosecond laser pulses for high-order harmonic generation. Two regimes were considered, namely Kerr effect-induced self-phase modulation broadening with seed pulses provided by Legend, and ionization-induced broadening with seed pulses provided by L1:Allegra. To validate our estimation of the experiment parameters, we conducted simulations using Matlab.

We designed the experimental setup and necessary diagnostic tools, implementing the 3D design using simulations in Zemax. The experimental setup and diagnostics were then built. Spectral broadening was successfully measured with two different laser sources, achieving all goals of the thesis.

This work required a deep understanding of non-linear optics and laser-matter interactions, as well as expertise in experimental design and implementation. The successful completion of the thesis objectives provides a benchmark for further development of the post-compression setup, bringing us closer to more efficient high-order harmonic generation. Future research could focus on optimizing the experimental setup and building the compression stage to provide compressed pulses to be used for HHG.

Bibliography

[1] BOYD, R. W., *Nonlinear optics*, Academic Press, 3rd edition, 2008

[2] FARACE, B., *Post-compression of high energy femtosecond pulses*, (Master's Thesis), Politecnico Milano, 2020

[3] ULTRAFAST INNOVATIONS, *Double-angle ultra-broadband compression mirrors*, (Product sheet), PC1332, 2023

[4] TREBINO, R., *Group velocity dispersion* [online], Ultrafast optics course, [cit. 15.8.2022], Available from: `https://frog.gatech.edu/talks.html`

[5] KAUMANNS, M. et al., *Multipass spectral broadening of 18 mJ pulses compressible from 13 ps to 41 fs*, Optics Letters, 2018, doi: 10.1364/OL.43.005877

[6] BOHMAN, S. et al., *Generation of 5 fs, 0.5 TW pulses focusable to relativistic intensities at 1 kHz*, Optical Society of America, 2008, doi: 10.1364/OE.16.010684

[7] NAGY, T. et al., *Generation of above-terawatt 1.5 cycle visible pulses at 1 kHz by post-compression in a hollow fiber*, Optics Letters 45, 3313-3316, 2020, doi: 10.1364/OL.395830

[8] TONG, X. M. et al., *Theory of molecular tunneling ionization*, Physical review A: Atomic, molecular and optical physics, 2002, doi: 10.1103/PhysRevA.66.033402

[9] HORT, O., *High harmonic generation with high energy femtosecond pulses*, L'Université de Bordeaux, 2014

[10] TREBINO, R., *Generation*, [online] Ultrafast Optics Short Course, [cit. 10.5.2023], Available from: `https://frog.gatech.edu/talks.html`

[11] PASCHOTTA, R., *Self-focusing* [online], RP Photonics, [cit 11.5.2023], Dostupné z: `https://www.rp-photonics.com/self-focusing.html`

[12] KASRA, A. et al., *Symphony on strong fied aproximation*, Reports on progress in physics, 2019, doi: 10.1088/1361-6633/ab2bb1

[13] HORT O. et al., *Postcompression of high-energy terawatt-level femtosecond pulses and application to high-order harmonic generation*, Journal of the Optical Society of America, 2015, doi: 10.1364/JOSAB.32.001055

[14] AUGUSTE, T. et al., *High-energy femtosecond laser pulse compression in single- and multi-ionization regime of rare gases: experiment versus theory*, Applied physics B: Lasers and Optics, 2013, doi: 10.1007/s00340-012-5309-x

[15] DUTIN, C. F. et al., *Post-compression of high-energy femtosecond pulses using gas ionization*, Optics Letters, 2010, doi: 10.1364/OL.35.000253

[16] NAGY, T. et al., *Generation of three-cycle multi-millijoule laser pulses at 318 W average power*, Optica 6, 1423-1424, 2019, doi: 10.1364/OPTICA.6.001423

[17] BREE, C. et al., *Method for Computing the Nonlinear Refractive Index via Keldysh Theory*, IEEE Journal of Quantum Electronics 46, 433-437, 2010, doi: 10.1109/JPE.2009.2031599

[18] BOHLE, F. et al., *Compression of CEP-stable multi-mJ laser pulses down to 4 fs in long hollow fibers*, Laser Phys. Lett. 11, 2014, doi: 10.1088/1612/2011/11/9/095401

[19] NISOLI, M. et al., *Generation of high energy 10 fs pulses by a new pulse compression technique*, Applied Phys. Lett., 1996, doi: 10.1063/1.116609

[20] JARNAC, A. et al., *Compression of TW class laser pulses in a planar hollow waveguide for applications in strong-fild physics*, The European Physical Journal, 2014, doi: 10.1140/epjd/e2014-50558-7

[21] JUYUN, P. et al., *Generation of 1.5 cycle 0.3 TW laser pulses using a hollow-fiber pulse compressor*, Optics Letters, 2009, doi: 10.1364/OL.34.002342

[22] SEDLACEK, O., *Post-compression of high power femtosecond laser pulses for high-order harmonic generation*, (Research Assignment), Czech Technical University, 2022

[23] STEVEN C. et al., *Frequency broadening by self-phase modulation in optical fibers*, Journal of the Optical Society of America B, 1985

[24] KELDYSH L. V. et al., *Ionization in the field of a strong electromagnetic wave*, Soviet physics JETP, 1964

[25] Ammosov M. V. et al., *Tunnel ionization of complex atoms and of atomic ions in an alternating electromagnetic field*, Soviet physics JETP, 1986

[26] TONG, X. M. et al., *Empirical formula for static field ionization rates of atoms and molecules by lasers in the barrier-suppression regime*, Journal of Physics B: Atomic Molecular and Optical Physics, 2005, doi: 10.1088/0953-4075/38/15/001